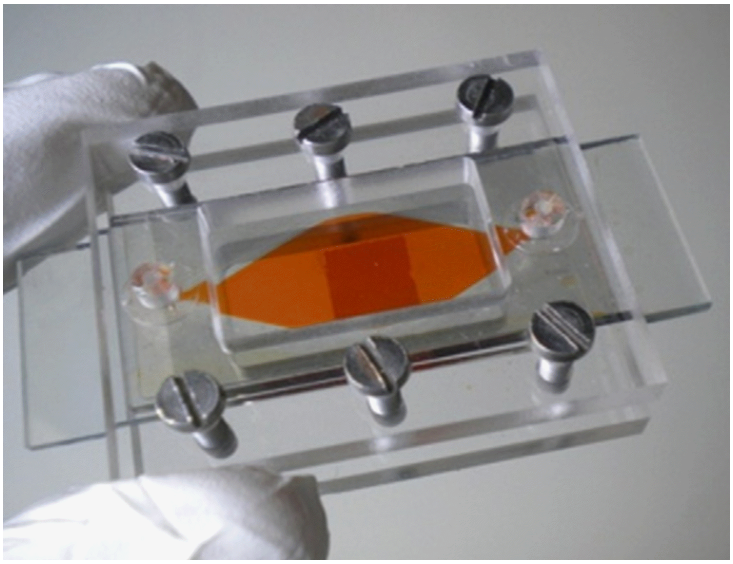

Figure 5.2: Photograph of the assembled type-I microfluidic-based DSC.

5.3 Type-I microfluidic DSC characterization

5.3.1 Fluidic tests

The experimental results on the sealing performances of the microfluidic architecture evaluated through the set-up depicted in Fig. 4.2 are reported in Fig. 5.3: pressure profiles inside the PDMS chamber as a function of the time show no temperature dependence for the selected pressures, both during liquid injection (rising ramp) and during the steady state regime. It is well known that air bubble inside a micro-structure expands during thermal cycles and could run out of the device through cavities and reversible interfaces [117]. In the case under study, for both pressure values, the plateau-like behavior of the curve is the evidence that no leakages occurred during the test. Moreover, the independence of the curves from temperature witnesses the absence of air bubbles formed in the chamber during liquid charging, as also confirmed by visual check. Thus, no volume expansion occurred, guaranteeing the optimal sealing for in-field operation.

It has to be noted that even if the membrane successfully prevents the electrolyte leakage, however it allows the air inlet into the microfluidic chamber, being the PDMS permeable to gases. For this reason the microfluidic architecture is particularly suitable only for quick tests on DSC constituent materials.

During cell fabrication, the microfluidic approach finds its immediate application in electrolyte filling. In fact, this procedure allows a controlled reagent release, since electrolyte can be delivered and removed in the already sealed architecture, avoiding waste and eluding the possible electrode deterioration thanks to a faster assembly process. Moreover, a useful application should also be found in dye sensitization of TiO_2. In fact, a more efficient impregnation, avoiding waste of expensive reagents and allowing in situ thermal processes can be simply implemented directly on-chip after cell assembly.

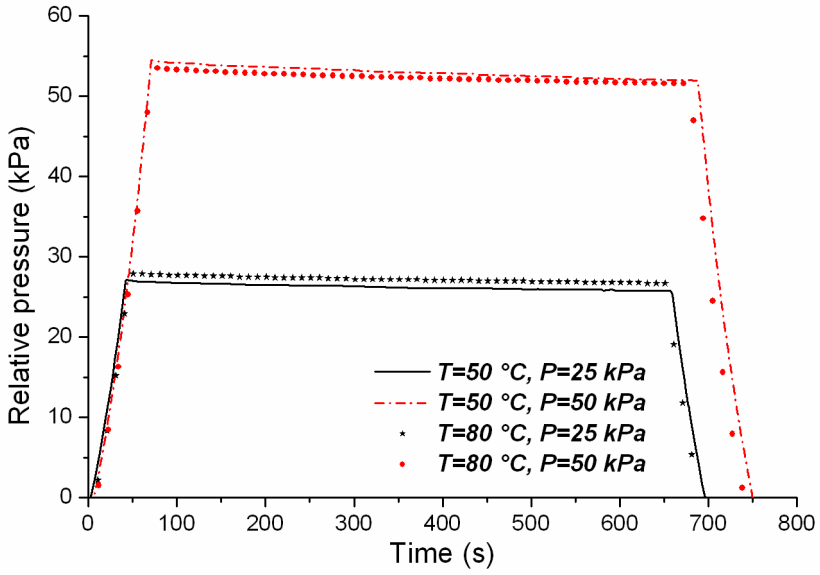

Figure 5.3: Fluidic leakage test at different temperature and pressure values.

Cell	J_{sc} (mA/cm^2)	V_{oc} (V)	FF	PCE (%)
Standard	12.39	0.670	0.64	5.1
Microfluidic	13.94	0.690	0.71	6.4

Table 5.1: Photovoltaic performances of standard-assembled and type-I microfluidic DSCs.

5.3.2 Photovoltaic performances

The photovoltaic performances of microfluidic DSCs fabricated by using standard photoanode, electrolyte and sensitizer, were evaluated through I-V characterization under AM1.5G illumination; the results were compared with the performances of DSCs assembled in non-irreversible way without microfluidic housing and closed by means of clips (referred to as *standard-assembled*). Representative results for the electrical characterization are shown in Fig. 5.4 and the evaluated photovoltaic parameters are reported in Table 5.1: as it is clearly evident, the microfluidic-based DSC exhibits a significant enhancement in short circuit current density (from 12.39 to 13.94 mA/cm^2). In all the measured samples, a mean efficiency increment of the 25% was obtained in microfluidic-based devices with respect to the standard-assembled ones.

This performance difference between the two kinds of harvesters was additionally evidenced by the impedance spectroscopy measurements, whose results are reported in Fig. 5.5. As explained in Section 3.5.2, the second semicircle of the impedance spectra is related to the electrolyte/photoanode recombination rate. The microfluidic devices thus show a clear improvement of the carrier lifetime, which is responsible for the enhanced efficiency with respect to the standard-assembled cells; in the meantime, no significant difference is observable in the counter electrode and electrolyte impedances.

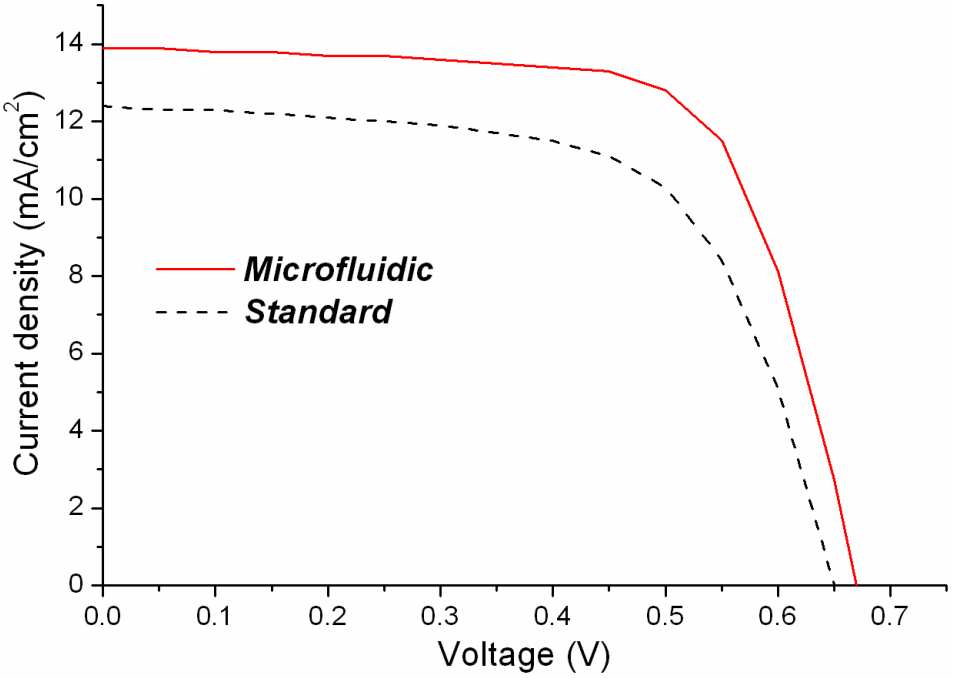

Figure 5.4: Current density-voltage curves of standard-assembled and type-I microfluidic DSCs.

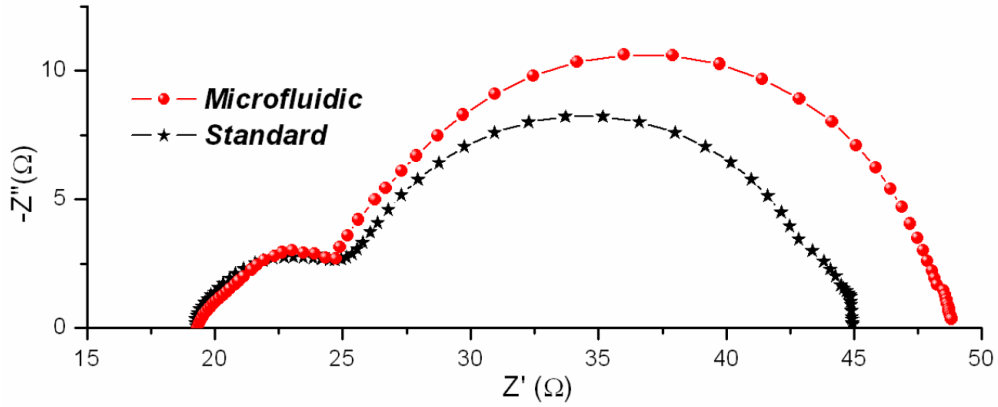

Figure 5.5: Electrochemical impedance spectra of standard-assembled and type-I microfluidic DSCs.

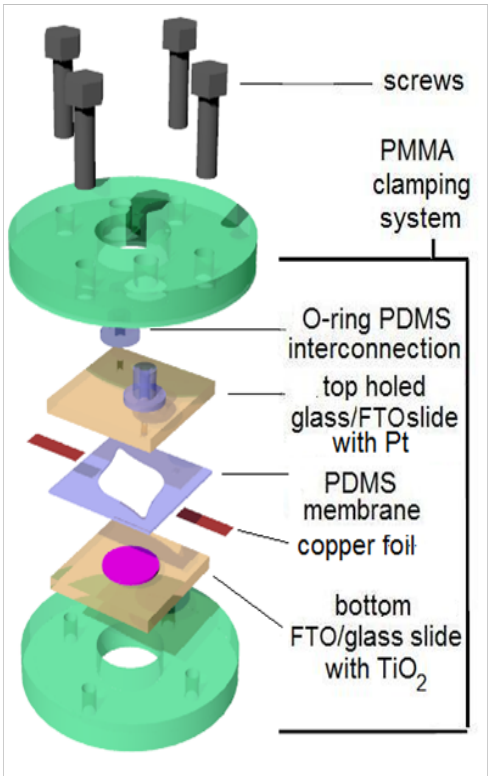

Figure 5.6: 3D sketch of type-II microfluidic-based DSC architecture.

5.4 Type-II structure

By using type-I architecture, some problems related to the mechanical endurance of the PMMA clamping system aroused, leading to the break of some electrodes during cell assembly. In order to overcome this issue, a modified architecture, named type-II, was proposed: the 3D sketch of this device is shown in Fig. 5.6.

In this case, by reducing the housing dimension and by using square glasses instead of rectangular ones, it was possible to balance the forces applied by the clamping system to the glasses by means of the screws, thus avoiding the electrode breaks. Moreover the chamber geometry was modified: it maintained the double-drop layout but its dimensions are reduced, thus decreasing the amount of electrolyte solution needed and also the TCO area that is not covered by TiO_2 and is then directly exposed to the electrolyte. In this case, since the uncovered TCO is responsible for electron recombination through the substrate (as explained in Section 3.5.1), a reduced area leads to a decrease of the chance of recombination through this path. Finally, in the new architecture a novel method was employed to provide the electric connections at the electrodes: instead of depositing silver paint directly onto TCO layer, copper foils, dielectrically isolated by the PDMS membrane, were used. As well as the previous architecture, also the type-II one sealing performances guarantee the electrolyte confinement and the absence of leakages.

In Fig. 5.7 a photograph of the assembled type-II microfluidic-based DSC is shown.

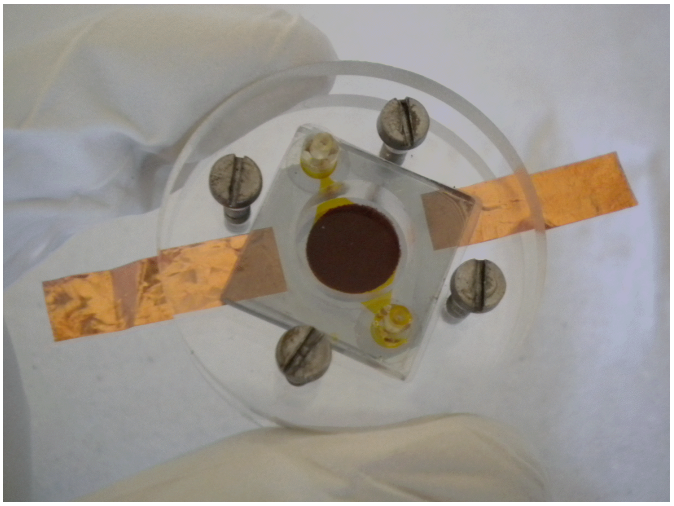

Figure 5.7: Photograph of the assembled type-II microfluidic-based DSC.

Membrane thickness (μm)	J_{sc} (mA/cm^2)	V_{oc} (V)	FF	PCE (%)
100	19.47	0.640	0.58	7.22
200	20.52	0.640	0.55	7.29

Table 5.2: Typical photovoltaic performances of type-II microfluidic DSCs fabricated with 100 μm-thick and 200 μm-thick PDMS membrane.

5.5 Type-II microfluidic DSC characterization

5.5.1 Reproducibility results

The microfluidic solar cells have been designed to permit control, reproducibility, and reliability in a simple system. Moreover, the reversibility of the sealing allows the inspection of the prototypes after usage. A significant attention has been devoted to the characterization of the reproducibility of the photovoltaic conversion efficiency. For this reason, a statistically significant number of identical cells were fabricated, and their photovoltaic performances were evaluated. In Fig. 5.8 the solar energy conversion efficiencies of 20 nominally identical microfluidic DSCs are reported: the average photoconversion efficiency is equal to 6.76%, with a standard deviation of 10%. The variation of the predicted efficiency value around the mean value is comparable with the best results obtained with irreversibly-sealed structures [20].

5.5.2 Cell thickness study

In order to study the effect of the membrane thickness on the performances of microfluidic DSC, I-V and EIS measurements were performed on two sets of devices, namely “thin” and “thick” cells, fabricated with 100 μm-thick and 200 μm-thick membrane, respectively.

The results of I-V characterization are resumed in Table 5.2: no significant difference in cell efficiency can be observed in the presented data, because the slightly higher short circuit current exhibited by the thicker cell is balanced by the enhancement of the fill factor for the device with

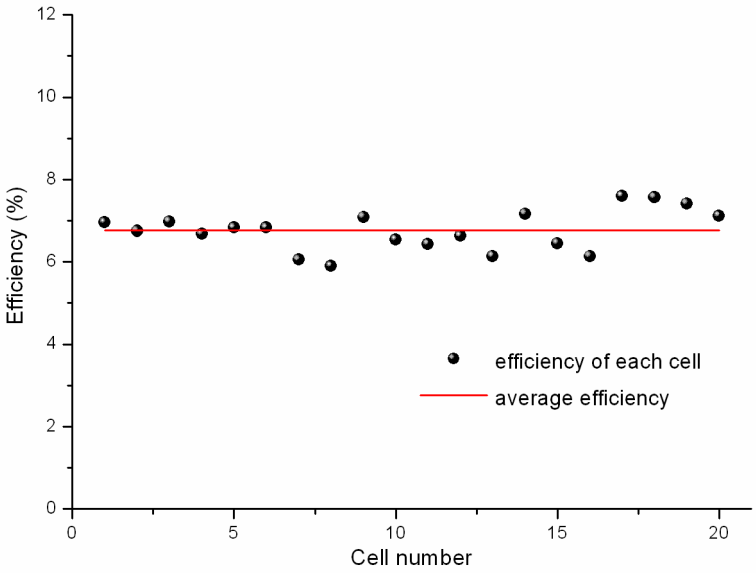

Figure 5.8: Evaluation of the photoconversion efficiency for 20 nominally identical type-II microfluidic cells.

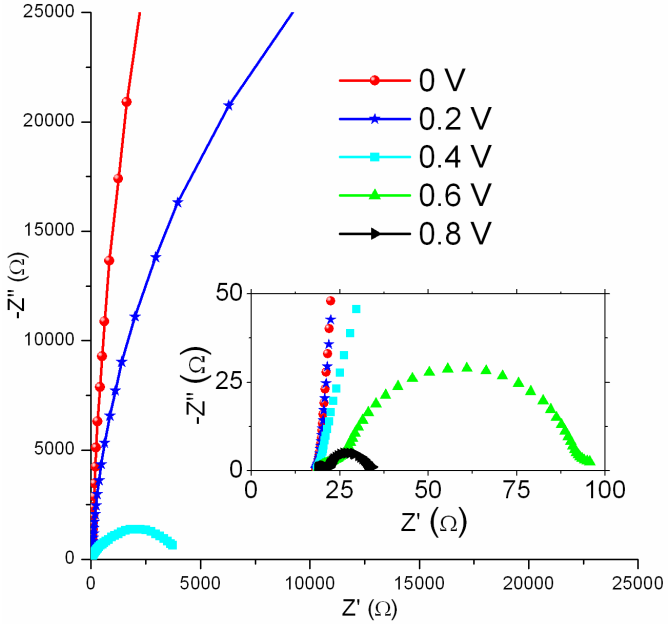

Figure 5.9: Impedance spectra of type-II microfluidic DSC fabricated with 200 μm-thick PDMS membrane acquired in dark conditions for different applied voltages. The high frequency magnification of the same curves is reported in the inset.

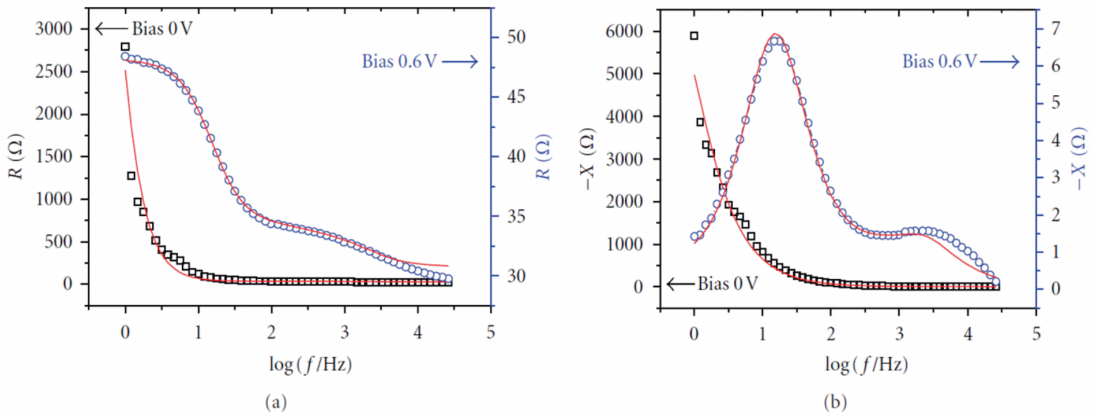

Figure 5.10: Real (a) and imaginary (b) parts of the impedance for the type-II microfluidic DSC fabricated with 200 μm-thick PDMS membrane under illumination. Black squares and blue circles are the experimental data for bias of 0 V and 0.6 V, respectively, while the continuous curves are the corresponding best fits.

thinner membrane. The increase of the FF value has to be expected, because the larger is the membrane thickness, the larger is the electrolyte diffusion resistance value (see Eq. 3.16), and this effect leads to an increase of the cell total series resistance, which is responsible for the lower fill factor [118]. However it has to be noted that the selected electrolyte thickness values are higher with respect to the ones used in non-fluidic devices (usually in the range 25 – 60 μm); this is due to the difficulty of fabricating PDMS membrane thinner than 100 μm. In Fig. 5.9 examples of Nyquist plots related to thick cell acquired in dark condition at different bias voltages are reported. In the graph the typical decrease of the central arc of the impedance plot for increasing voltage values can be appreciated, evidencing the charge transfer resistance dependence on the applied potential (see Section 3.5.1).

The experimental data were fitted by using the model described in Section 3.5.1. Some examples of the fitting results are reported in Fig. 5.10 for the thicker cell under illumination. Regarding the Bode plot of the real part of the impedance (Fig. 5.10a), in short circuit condition it exhibits a monotonic behavior as a function of the frequency, while at 0.6 V two features can be observable, one at higher frequency (above 1 kHz, ascribable to counter electrode impedance) and the other one in the range 1 - 100 Hz (related to TiO_2/electrolyte interface impedance). The same information can be obtained from the imaginary part of the impedance plotted in Fig. 5.10b.

In order to investigate the dependence of the photoanode/electrolyte interface impedance on the bias voltage, the best fit parameters R_{ct} and C_μ, characterizing this interface, were evaluated. Their behaviors as a function of the applied potential are shown in Fig. 5.11a and Fig. 5.11b, for the cells under illumination; the triangles and stars refer to membranes of thicknesses 100 μm and 200 μm, respectively. Is it worthy to note that these quantities weakly depend on the thickness of the DSC, as expected, as they have to describe interface properties. The bias voltage dependence of R_{ct} and C_μ is well described by the TLM according to which [118]:

$$R_{ct} = R_0 e^{-\rho \frac{V}{V_{th}}} \tag{5.1}$$

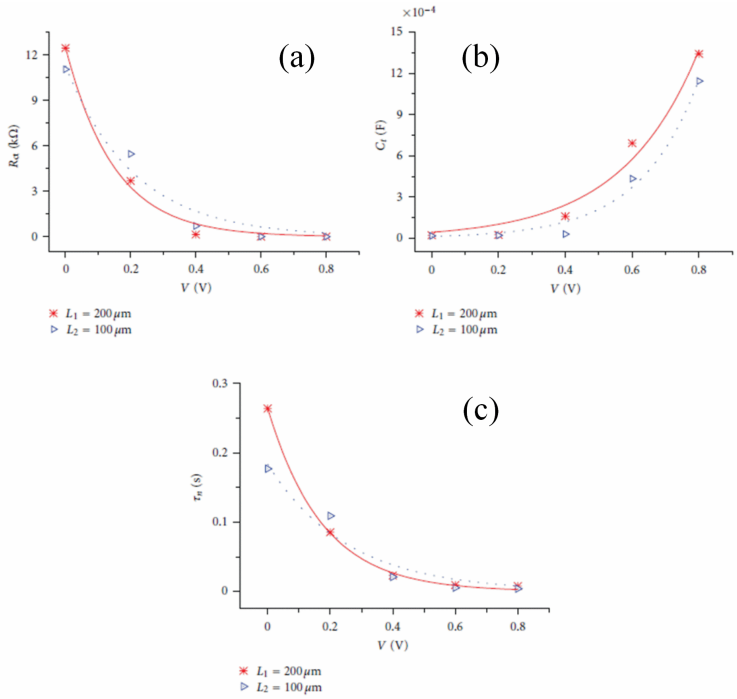

Figure 5.11: Recombination resistance (a), chemical capacitance (b), and charge lifetime (c) versus applied bias voltage for type-II microfluidic DSCs fabricated with 100 μm-thick (blue triangles) and 200 μm-thick (red stars) PDMS membrane, under light conditions. The continuous curves are the best fit.

$$C_\mu = C_0 e^{\sigma \frac{V}{V_{th}}} \tag{5.2}$$

where R_0 and C_0 are the resistance and capacitance of the interface at 0 V bias, and ρ and σ are two constants. From the best fit of Fig. 5.11a and Fig. 5.11b ρ and σ values were calculated, and the results are summarized in Table 5.3. The difference between ρ and σ may be explained by the fact that R_{ct} depends on the free contact surface between the titania and the electrolyte (i.e. the total surface of the pore minus the surface occupied by the adsorbed dye molecules) whereas C_μ depends on the total surface of the pore (considering that the adsorbed dye molecular film minimally alters the dielectric constant in the interface). By means of the measured R_{ct} and C_μ values, exploiting the formula 3.11, the electron lifetime was evaluated and it is reported in Fig. 5.11c. From this figure, it follows that τ_n is practically independent on the thickness of the DSC and depends on the bias in an exponential manner, as it follows from the expressions 5.1 and 5.2.

In addition, the chemical diffusion coefficient and the diffusion length were evaluated starting from the fitting parameters. For example, for the cell with 200 μm-thick membrane at 0.6 V, values of D_n equal to $8 \cdot 10^{-5}$ cm^2/s and of L_n equal to 8.4 μm were obtained; both of them are in good agreement with results reported in literature for non-fluidic devices [98, 107].

Membrane thickness (μm)	ρ	σ
100	0.13	0.15
200	0.17	0.11

Table 5.3: Dependance of ρ and σ on PDMS membrane thickness.

5.6 Conclusions

In this chapter, an innovative microfluidic housing system for DSCs has been proposed. The aim of the work was the engineering of a small laboratory device which permits to distinguish between the contributions of the different components and technological steps. The microfluidic structure is constituted by all the components of a common DSC with the addition of a PDMS membrane sandwiched between the electrodes, that is used to retain the electrolyte solution; the structure can be reversibly sealed by means of a housing system consisting of mechanical clamping, inlet/outlet ports and interconnections to external fluids handling devices. This new proposed design effectively confines the liquid electrolyte in the final device, improving the life and the performance of the prototype by preventing failure due to electrolyte leakage or solvent evaporation. Application of microfluidic concepts in DSC architecture is also functional in order to overcome intrinsic problems faced during cell fabrication process.

The sealing performances of the housing test cell were characterized at different operating pressures and temperatures. Good sealing for pressure up to 50 kPa and temperature of 80 °C was obtained, avoiding leakage and bubble formation. I-V electrical characterization under illumination and impedance spectroscopy measurement showed a performance improvement with respect to DSC prototypes fabricated following the standard procedure.

A modified architecture (type-II structure) has been afterwards proposed, in order to overcome some cell fabrication weak points. This technological approach guaranteed also a high degree of fabrication reproducibility, as demonstrated by a statistical analysis.

By using the type-II structure a study on the effect of the membrane thickness was performed. No significant difference was evidenced by varying this parameter, but the EIS analysis showed that the transmission line model (widely used in literature for non-fluidic DSC) can be successfully applied also to microfluidic devices. In fact, the experimental data are well described by the TLM and the parameters characterizing the diffusion coefficient and the diffusion length of the carrier in the TiO_2 layer are in agreement with the values reported in the literature. This validation is fundamental since it shows that the microfluidic approach does not change the nature of the device, but simply adds flexibility and reliability, thus demonstrating the effectiveness of the microfluidic cell as a standard modular prototype which can be used for testing different DSC components.

Chapter 6

Microfluidic DSC applications

6.1 Introduction

In the previous chapter, the novel proposed microfluidic architecture was demonstrated to be effective as a modular prototype for small laboratory DSC fabrication. The structure allows the fast assembling of the devices with a very high degree in fabrication reproducibility and the possibility to inspect the device components after usage thanks to the reversible sealing. This chapter describes how the peculiarities of this architecture were exploited in the test of different innovative DSC components, with a very low amount of waste reagents and materials.

First of all, different novel organic dyes were tested as sensitizers, and the photovoltaic performances of the fabricated solar harvesters were evaluated. The attention was then focused on the study of one of these new dyes, namely the hemi-squaraine sensitizer, whose photovoltaic properties and recombination characteristics in DSC were studied and improved. Moreover innovative photoanode materials such as sponge-like ZnO nanostructures and anodically-grown TiO_2 nanotubes were tested in microfluidic devices. Their photovoltaic performances and transport properties were studied and the results were compared to standard photoanodes based on TiO_2 nanoparticles. Finally, one of the best applications of the microfluidic structure was found in the non-destructive analysis of DSC components over time. In fact, thanks to the possibility to open and close the housing system, it became possible to study the behavior of each cell element during usage without compromising the device integrity. For this reason, a study aimed to demonstrate the possibility of performing non-destructive analysis of cell components will be presented.

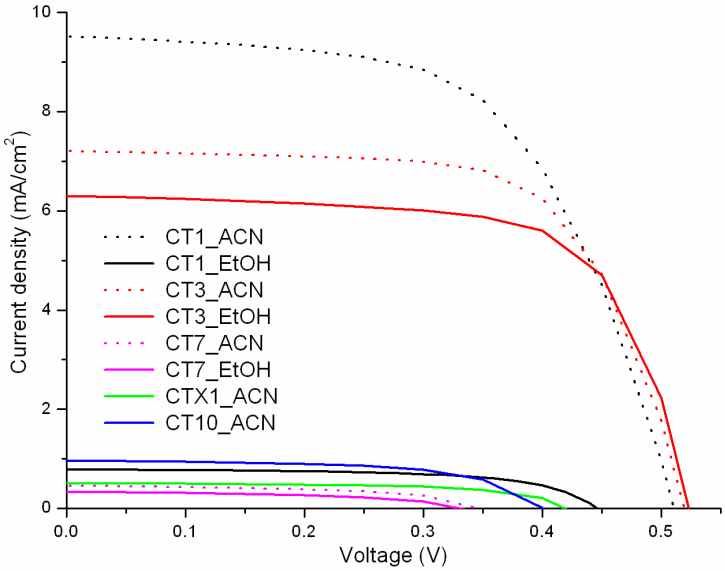

Figure 6.1: Current density-voltage curves of organic dye-based microfluidic DSCs (ACN = acetonitrile, EtOH = ethanol).

6.2 Testing of novel organic sensitizers

As already mentioned in Section 2.1.3, metal-based sensitizers exhibit some limits. The relatively low molar extinction coefficient in the visible region requires an increase of the TiO_2 layer thickness in order to absorb a significant fraction of the incident light. Moreover, the most commonly used element, the ruthenium, is a noble metal, unsuitable for large-scale industrial production, since its availability is limited, its employment is not cost effective and it opens potential environmental issues related to waste disposal [119]. With this respect, metal-free organic dyes present several advantages since they are usually characterized by high molar extinction coefficients, and, in principle, can be produced with simple, fast and cost effective synthetic approaches.

In the following, a report on the testing of five novel organic sensitizers produced by Cyanine Technologies s.r.l. in the framework of a collaborative project will be presented. A preliminary study aimed to select the sensitizers with the most promising features was carried out by means of I-V electrical characterization under AM1.5G simulated sunlight. Based on the results of this screening, the most performing sensitizer was chosen, and a detailed study based on the evaluation of optical, electrical and electronic properties of solar devices fabricated with the selected dye was performed.

6.2.1 Preliminary screening on organic dyes

The preliminary screening on the organic sensitizers was performed employing five dyes, by studying also the effect of the solvent used to prepare the sensitizing solutions. For this reason the dyes named CT1, CT3 and CT7 were tested employing acetonitrile (ACN) and ethanol (EtOH) as solvents, while CTX1 and CT10 were only tested by dissolving them in ACN.

The results of the photovoltaic characterization are reported in Fig. 6.1 and the photovoltaic

Dye	Solvent	J_{sc} (mA/cm^2)	V_{oc} (V)	FF	PCE (%)
CT1	ACN	9.52	0.51	0.59	2.88
CT1	EtOH	0.78	0.45	0.63	0.22
CT3	ACN	7.21	0.52	0.67	2.50
CT3	EtOH	6.30	0.52	0.68	2.24
CT7	ACN	0.46	0.35	0.55	0.09
CT7	EtOH	0.34	0.33	0.49	0.06
CTX1	ACN	0.51	0.42	0.62	0.13
CT10	ACN	0.97	0.40	0.61	0.24

Table 6.1: Photovoltaic performances of organic dye-based microfluidic DSCs (ACN = acetonitrile, EtOH = ethanol).

parameters are summarized in Table 6.1. As it is clearly noticeable, the best photovoltaic performances were obtained by using CT1 dye dissolved in ACN, but also CT3 showed discrete photoconversion efficiencies, equal to 2.5% and 2.24%, when dissolved in ACN and EtOH, respectively. On the other hand, the remaining sensitizers do not exhibit valuable efficiencies. Moreover a general comment on the effect of the solvent can be made: for all the sensitizers under study, the photovoltaic performances of the devices fabricated by dissolving the dye in ACN are higher with respect to those dissolved in EtOH, indicating a non-complete dissolution in the latter. Few words need to be spent about the CT1 dissolved in ethanol: in this case the efficiency value is very low (0.22%) if compared to the same dye dissolved in ACN (2.88%). The main reason for this reduced efficiency could be the esterification of the sensitizer when it is dissolved in a protic solvent like ethanol, which limits the anchoring of the dye to the semiconductor surface.

6.2.2 Study on hemi-squaraine dye

By looking at the results reported in Table 6.1 for the DSCs fabricated with the organic sensitizers, the best results were obtained by using CT1 dissolved in acetonitrile solution. For this reason, this dye was chosen in order to carry out a detailed study of the photovoltaic properties and recombination characteristics of solar harvesters based on its use.

In the following, the effectiveness of this dye, which belongs to a relatively new photosensitizer's class, namely the hemi-squaraine molecule, will be studied. Although squaraine dyes are well known in DSC [120], its hemi-squaraine intermediate has been rarely proposed [121] and never well studied as TiO_2 sensitizer. Indeed this dye, beside its simplicity, its small dimension and its quite reduced absorption energy range, can be efficiently employed in DSCs. One of the peculiar features that makes hemi-squaraines a unique class of sensitizer is their anchoring group, the squaric acid moiety. The molecular structure of the hemi-squaraine dye is reported in Fig. 6.2.

The study of structural and electronic coupling between hemi-squaraine and TiO_2, focused on the role of the anchoring group, was performed by means of theoretical calculations based on Density Functional Theory (DFT) and Time Dependent DFT (TDDFT), and it is reported in details in ref. [49]. Briefly, the results showed that the relatively high efficiency of the hemi-squaraine

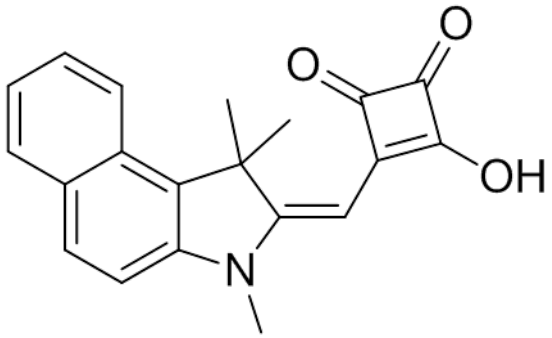

Figure 6.2: Molecular structure of the hemi-squaraine sensitizer.

dye could be ascribed to a large displacement of electron charge towards the anchoring group in the excited state and to a strong chemical bonding between the squarate moiety of the dye and the anatase surface, which also induces hybridization between the unoccupied molecular states of the dye and the surface atoms of the oxide, revealing adiabatic electron transfer mechanism. In order to verify if CT1 can work as TiO_2 sensitizer, the alignment of the dye molecular levels with respect to the oxide band structure was determined experimentally by cyclic voltammetric analysis, also reported in ref. [49]. This analysis showed the formation of a staggered interface (see Section 2.1.3), that is responsible for an efficient electron injection into the semiconductor CB.

Since the predictions of the *ab initio* calculations showed that the requirements for efficient application of CT1 in solar cells were satisfied, the sensitization of a TiO_2 nanoparticle network was experimentally characterized. Moreover the effect of the chenodeoxycholic acid (CDCA), employed as co-adsorbent in order to reduce dye aggregation at the TiO_2 surface, was studied, by adding it in different concentrations (1 and 10 mM, corresponding to 4:1 and 40:1 concentration ratio between the CDCA and the dye, respectively) in the sensitizing solution. CDCA has also a strong influence of the quantity of the adsorbed dye since it competitively saturates the anchoring sites present at the surface. The impregnation time was fixed to 5 h. For comparison, a reference photoelectrode obtained with overnight impregnation of the oxide layers with a 0.3 mM N719 dye solution was fabricated and characterized.

Figs. 6.3a and 6.3b compare the absorption spectrum of the dye in acetonitrile solution and those obtained for the TiO_2 photoanodes, respectively. The latter spectra exhibit an absorption range that is broader and red-shifted with respect to the dye in solution independently on the presence of CDCA. These results are confirmed also by incident photon-to-electron conversion efficiency (IPCE) spectra reported in Fig. 6.3c which show a surprisingly large red-shifted on-set (for a yellow dye having a maximum centered at 430 nm) around 600 nm. Both the broadening and the shift (blue or red depending on the dye characteristics) are commonly observed in spectral responses of organic dyes attached to the TiO_2 surface and they are generally attributed to the interaction of the anchoring group with the substrate surface, and/or to the formation of dye aggregates [122]. In this case, no strong dependence of the red shift on the presence of a co-adsorbent can be observed, thus it cannot be related with dye aggregation. Moreover the relatively high IPCE values demonstrate that the dye effectively injects electrons into the oxide conduction band as suggested

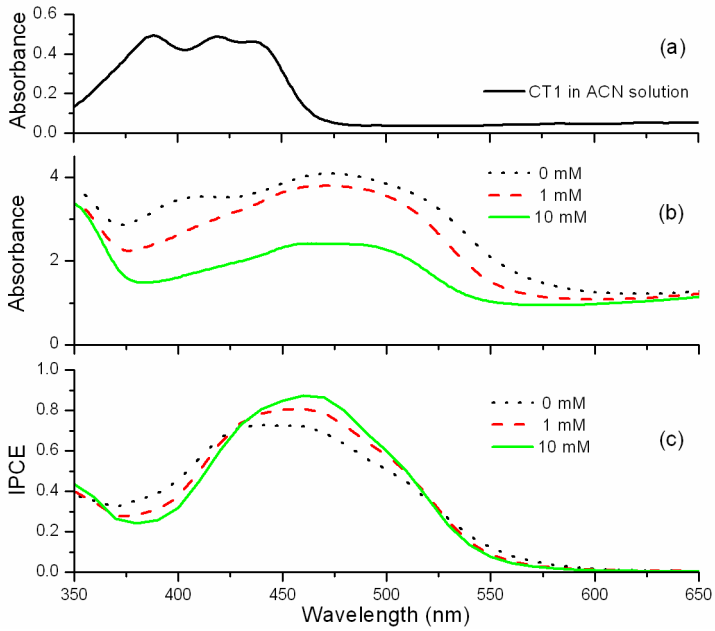

Figure 6.3: UV-visible absorbance spectra obtained for hemi-squaraine dye in acetonitrile solution (a) and for the dye attached to the nanocrystalline TiO_2 layer for different CDCA concentrations (b). IPCE curves of hemi-squaraine solar cells for different CDCA concentrations (c).

Dye	CDCA (mM)	J_{sc} (mA/cm^2)	V_{oc} (V)	FF	PCE (%)	τ_n (ms)
CT1	0	7.68	0.55	0.64	2.74	10.68
CT1	1	7.82	0.61	0.69	3.32	15.25
CT1	10	7.89	0.64	0.70	3.54	21.74
N719	0	15.68	0.62	0.65	6.33	12.46

Table 6.2: Photovoltaic performances of microfluidic DSCs sensitized by CT1 and N719 dyes for different CDCA concentration evaluated from I-V characterization and EIS analysis.

by DFT electronic structure study. Fig. 6.3 also reveals the beneficial effects of the co-adsorbent, whose presence leads to higher, narrower and slightly red-shifted peaks in the IPCE spectra (Fig. 6.3c), reaching the maximum value of 87% around 470 nm for a 10 mM CDCA concentration. CDCA molecules act as spacers among the hemi-squaraine molecules, avoiding dye aggregation and thus facilitate electron injection into the semiconductor CB. In the absorption spectra of Fig. 6.3b, a lower dye loading induced by CDCA presence is evident, together with the disappearance of a shoulder at about 395 nm. The shoulder, not present in the IPCE spectra, can be attributed to dye molecules aggregates which are not contributing to charge generation and whose formation is inhibited by CDCA.

The results obtained under AM1.5G illumination for the I-V and the electrochemical impedance spectroscopy measurements at open circuit voltage are summarized in Table 6.2 and reported in Fig. 6.4; the Bode representation of impedance phase of the cells is also shown in the inset of Fig. 6.4. By fitting the EIS experimental data, the values of the electron lifetime τ_n were calculated and they are reported in Table 6.2. An analysis of the photovoltaic characterizations reveals a photo-

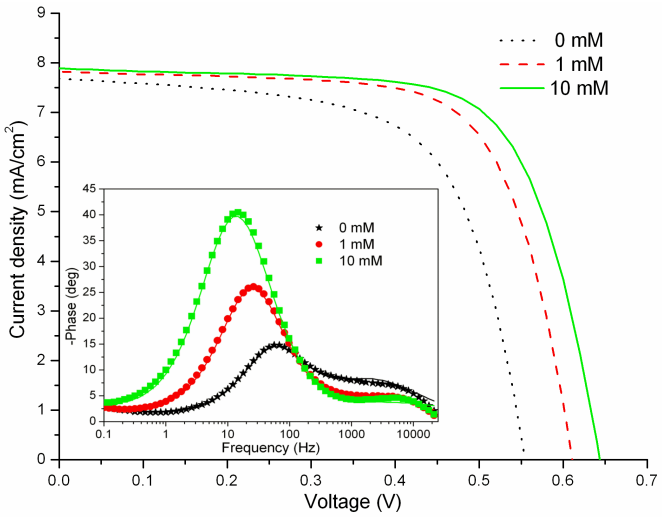

Figure 6.4: Current density-voltage curves of hemi-squaraine based solar cells for different CDCA concentrations. The corresponding Bode plots of EIS phase are shown in the inset (the points are experimental data while the continuous lines are fitting curves).

conversion efficiency of 2.74% without co-adsorbent, which becomes 3.54% when adding CDCA at 10 mM concentration. This efficiency is lower than the one obtained for the reference cell with N719 (6.33%), yet it has to be highlighted that one of the main technological steps that may require further optimization is the impregnation time of the nanostructured titania that was currently fixed to 5 hours. This time interval is quite short if compared to those required by Ru-based dyes but already gives satisfactory cell performances. This result indicates that the attachment of the hemi-squaraine dye to the TiO_2 surface is fast, in agreement with the theoretical calculations predicting a strong interaction of the squaric acid group with anatase. This aspect is very important since reducing the soaking time would lead to important technological advantages during cell fabrication.

In Table 6.2 it is also possible to note that both the open circuit voltage, V_{oc}, and the short circuit current density, J_{sc}, values increase when using the coadsorbent acid. The current density increase can be attributed to the improved electron injection efficiency [123] following dye disaggregation. The increase of V_{oc} can be explained by examining the τ_n values reported in Table 6.2 and the Bode plots shown in the inset of Fig. 6.4. Upon CDCA adsorption, surface TiO_2 trap sites are occupied by the acid molecules and consequently the CDCA causes an increase of the lifetime (also witnessed by a corresponding shift of the middle frequency peak of the Bode plot towards lower frequency values). Considering that τ_n increases with CDCA, the V_{oc} increase has to be related to a decrease of back electron transfer recombination due to the fact that the TiO_2 trap sites are occupied by the acid molecules [124].

6.3 Sponge-like ZnO based photoanodes

As introduced in Section 2.1.2, zinc oxide is well known as a promising alternative to titanium dioxide for the fabrication of photoanodes in DSCs. One of the most important features of this

material is its ability to easily grow in a wide variety of nanostructures. The possibility to change the morphology at the nanoscale can open wide opportunities in the control of charge transfer dynamics in the photoelectrode. In fact, by opportunely tuning the morphology, it is possible to combine the fast direct transport in 1D or quasi 1D nanostructures (like nanowires and nanorods) with the wide exposed area for dye sensitization typical of mesoporous layers. For this reason, in the last years the efforts of many research groups were devoted to investigate 3D structures, such as branched and dendritic nanowires [125, 126] in order to find the ideal equilibrium between direct electron transport and availability of a high number of light adsorbing molecules.

However, one of the most challenging task in order to obtain high performance ZnO photoelectrodes is probably the efficient coverage with dye molecules, because the surface chemistry of ZnO is basically different from that of TiO_2, and this is mirrored in a different sensitization behavior. For example, the dye loading on ZnO employing Ru complexes is influenced by a long-term surface degradation, and the residence time in dye solution influences the photoelectrochemical output of the cell [127]. Long incubation times cause the formation of aggregates between dye molecules and dissolved Zn^{2+} ions originating from the ZnO surface [128]. Such aggregates fill up the pores of the ZnO nanostructures without injecting electrons in the semiconductor, reducing the overall efficiency of the device. Sensitization procedure needs to be optimized in order to avoid ZnO surface damaging and molecular aggregate formation. At present, then, the light-to-electricity conversion efficiencies of ZnO-based DSCs are relatively low with respect to TiO_2 based devices, arriving to 6% only for small area laboratory cells based on mesoporous nanoparticle network [29, 129]. Hence, the improvement of the cell performance is still a challenging task and there is room for suggesting new architectures in view of increasing the efficiency values.

In the following, the fabrication and characterization of dye-sensitized solar cells with ZnO-based photoanodes with valuable efficiency will be presented. A simple, low cost and scalable method for the deposition of sponge-like mesoporous ZnO nanostructures was used, based on the deposition of a nanostructured Zn film on glass covered with fluorine-doped tin oxide by RF magnetron sputtering technique and subsequently subjected to a thermal treatment in oxygen atmosphere. Crystalline phase, quality, and morphology of the film were investigated. The dependence of the cell efficiency on dye incubation time and film thickness was studied with by means of I-V electrical characterization, IPCE and EIS measurements.

6.3.1 Photoanode characterization

In Fig. 6.5a the morphology of the deposited film as evaluated by FESEM is presented. The Zn film shows a sponge-like structure, compatible with the results presented in literature for Zn-Al coatings [130]. The nanostructuring of a metallic film in a sponge-like structure occurs for growth processes performed with a substrate temperature T approximately equal to a half of the melting temperature T_m [131]. Being the melting temperature for zinc particularly low ($\sim$690 K), the substrate temperature required for obtaining a value of $0.5T_m$ is about 350 K. Since the substrate temperature can increase by tens of degrees during sputtering deposition because of the energy released by incident particles [132], the conditions for obtaining such a nanostructure are easily

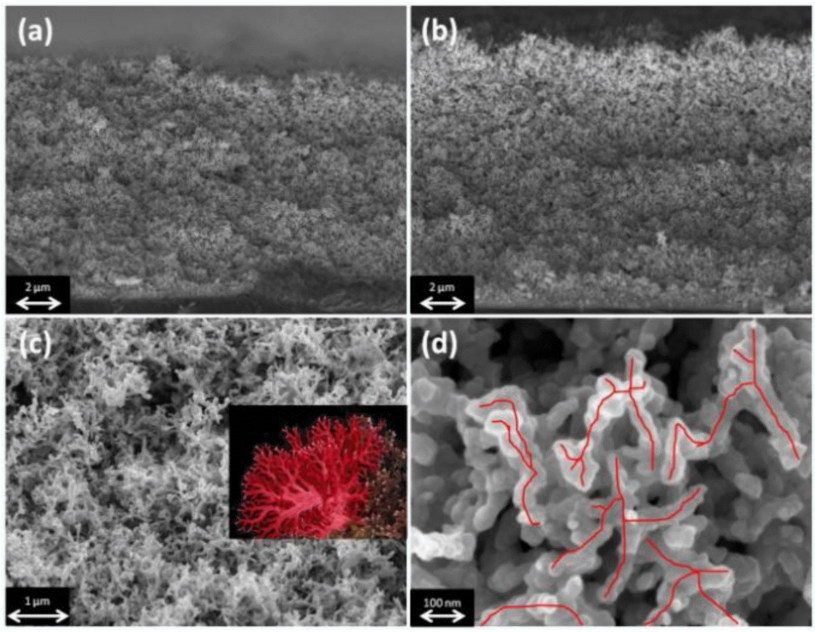

Figure 6.5: Sponge-like Zn-ZnO FESEM characterization: (a) Zn film, cross view; (b) ZnO film, cross view; (c) ZnO film, top view, and (inset) visual comparison with a natural coral; (d) magnified image of the sponge-like morphology, where the branched structure is evidenced.

achieved with no intentional heating. As depicted in Fig. 6.5b, no significant morphological variation can be noticed after the high temperature oxidation procedure, resulting only in a moderate volume expansion. Top view in Fig. 6.5c allows appreciating the porous morphology of the film and its similarity with the structure of natural coral. The specific exposed surface, as measured by Brunauer-Emmett-Teller (BET) method, was equal to 14.1 m^2/g, in line with what measured for mesoporous ZnO layers deposited with other techniques [29]. On the magnified FESEM picture in Fig. 6.5d it is possible to observe the 3-dimensional coral-like nanostructure, formed by the superimposition of small branches able to grow in length along basically every direction. The typical dimension of the particulate is around 40 nm, with spacing between adjacent structures in the range 10 – 60 nm. Taking into account that the typical exciton length in ZnO is in the range 5 – 20 nm, such morphological feature presents all the desired characteristics for efficient dye loading and charge transport towards the electrode [129].

The macroscopic appearance of the deposited film before and after the oxidation treatment drastically changes, moving from a black to a transparent feature, as shown in Fig. 6.6a. In Fig. 6.6b, the X-ray diffraction characterization of the film before and after the oxidation procedure is reported. The diffraction pattern after the thermal treatment witnesses a complete oxidation of the film, with a pure wurtzite crystalline structure, evidencing the absence of Zn residuals, which could be detrimental for the charge transport in DSC photoelectrodes.

6.3.2 Photovoltaic performances

In order to study and optimize the photovoltaic performances of the sponge-like ZnO photoanodes, different dye immersion times, different pH of the sensitizing solution, and different film

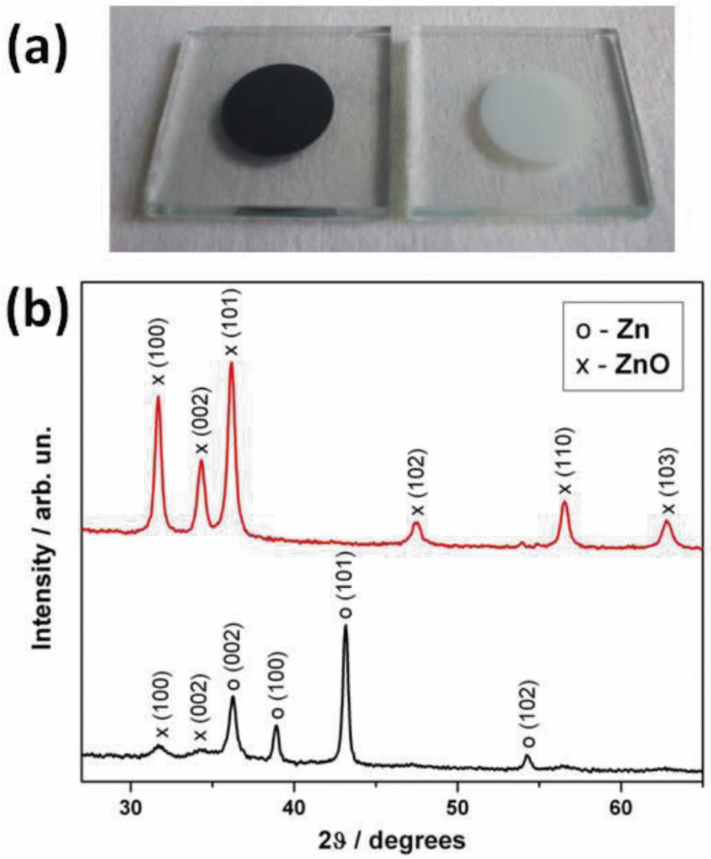

Figure 6.6: (a) Picture of the photoanode, before (left) and after (right) the oxidation treatment; (b) XRD characterization, before (black pattern) and after (red pattern) the oxidation treatment (JCPDS cards: Zn 87-0713, ZnO 89-1397).

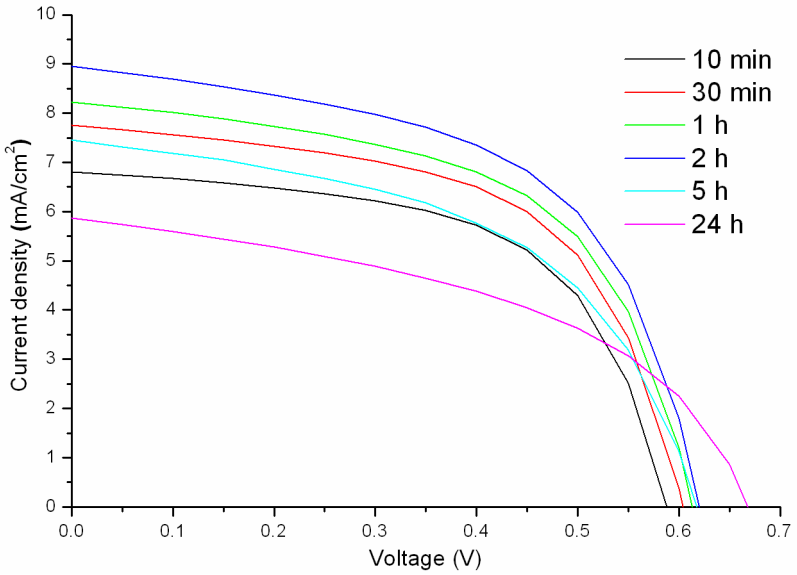

Figure 6.7: Current density-voltage curves of sponge-like ZnO-based DSCs for different impregnation times in dye solution; the thickness of the ZnO layer is 5 μm.

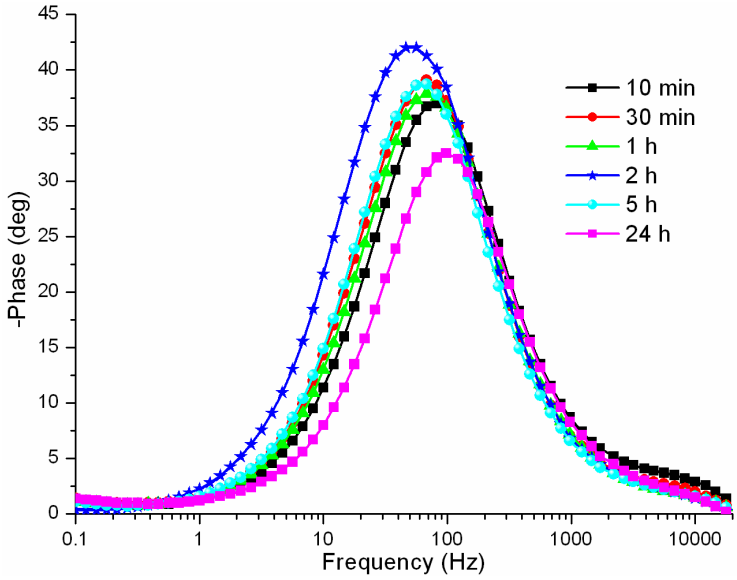

Figure 6.8: Bode plot of phase impedance of sponge-like ZnO-based DSCs for different impregnation times in dye solution measured at cell V_{oc}; the thickness of the ZnO layer is 5 μm.

thicknesses were tested.

In Fig. 6.7 and Fig. 6.8 the experimental curves for current density versus voltage analysis and impedance spectroscopy characterization for cells fabricated with 5 μm-thick ZnO photoanodes subjected to different immersion times in N719 solution (ranging between 10 min and 24 h) are reported, and the evaluated photovoltaic parameters are presented in Table 6.3. The PCE values are reported in Fig. 6.9 as a function of the incubation time in dye solution. It emerges a non-monotonic behavior with a most favorable sensitization time of 2 h. The lowering of cell efficiency during prolonged treatments is caused by a progressive degradation of ZnO surface. In fact, the modeling of EIS spectra evidences an initial decrease of the rate constant related to electron recombination as emphasized in Fig. 6.9 (in Fig. 6.8 the phase peak related to the recombination shifts towards low frequencies for loading time lower than 2 h). For immersion times longer than the optimal value, the recombination processes related to the interface between the unsensitized zones of the oxides and the electrolyte gain importance, as it is witnessed by the shift of the phase peak towards higher frequencies, i.e. lower lifetime values, as described in Section 3.5.1. The initial rise in efficiency for short incubation times is related to the slow kinetic of dye adsorption on the semiconductor surface. For low coverage of ZnO surface with dye molecules, the efficiency is reduced both because the number of photogenerated carriers is lower and because the recombination between the unsensitized ZnO and the electrolyte is higher. The unoccupied dye-absent sites on semiconductor surface are supposed to increase the rate of interfacial electron transfer (recombination) from the conduction band of ZnO to I_3^-. The decrease in efficiency when the optimal incubation time is exceeded can be related to the formation of molecular aggregates between dye molecules and dissolved Zn^{2+} ions originating from the ZnO surface. The aggregates give rise to a filtering effect (inactive dye molecules) as reported in literature [127]. In particular, the following three mechanisms are involved: adsorption of dye, dissolution of Zn surface ions,

Dye impregnation time	J_{sc} (mA/cm^2)	V_{oc} (V)	FF	PCE (%)	ω_n (s^{-1})
10 min	6.81	0.59	0.58	2.47	518
30 min	7.75	0.60	0.58	2.84	468
1 h	8.23	0.62	0.58	2.99	398
2 h	8.95	0.62	0.57	3.09	322
5 h	7.45	0.62	0.52	2.50	491
24 h	5.87	0.67	0.48	1.90	613

Table 6.3: Photovoltaic performances of sponge-like ZnO-based DSCs for different impregnation times in dye solution evaluated from I-V characterization and EIS analysis; the thickness of the ZnO layer is 5 μm.

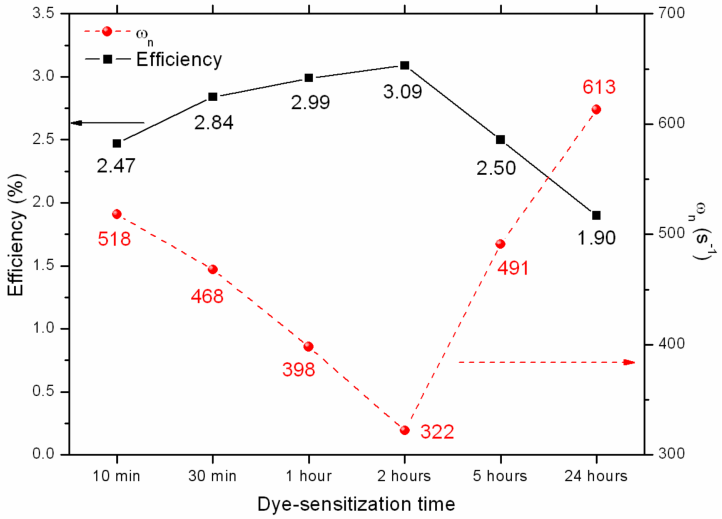

Figure 6.9: Efficiency behavior of 5 μm ZnO-based DSCs with different impregnation time in dye solution. The corresponding oxide-electrolyte interfacial rate constants for recombination ω_n obtained by fitting the impedance spectra are also shown.

and formation of aggregates in the pores of the film.

In order to better analyze the Zn^{2+}/dye aggregates formation, optical absorbance measurements in the UV-visible range were performed on the sensitized ZnO photoanodes for different soaking times. The resulting spectra are reported in Fig. 6.10. The typical N719 adsorption peaks (located at 400 and 535 nm) clearly increase while increasing the impregnation time from 10 min to 5 h, as confirmed visually by the color of the film, which becomes more intense for longer dipping. After 24 h of incubation, the behavior of the absorbance curve drastically changes; the overall increase in absorbance evidences a higher content of dye molecules, but the shift of the peak at 400 nm and the arising of new peaks (as shoulders of the peak centered at 535 nm) indicate the formation of new aggregates. Such molecular complexes show strong adsorption properties but are unable to inject electrons in the conduction band of the semiconductor as confirmed by IPCE spectra reported in Fig. 6.11. In fact, the curve related to 24 h of incubation time shows the lowest values of IPCE, whereas the 2 h cell shows the best performance.

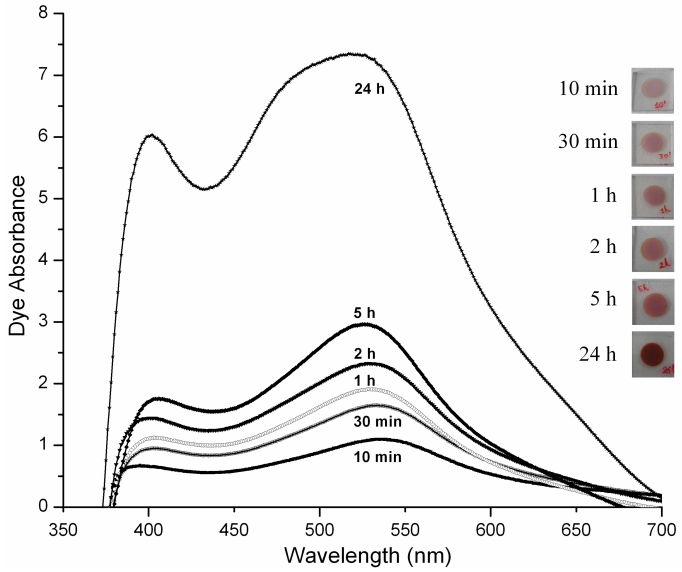

Figure 6.10: UV-visible absorbance curves obtained for the N719 dye on the sponge-like ZnO photoanodes (shown in the inset) for different incubation times in dye solution.

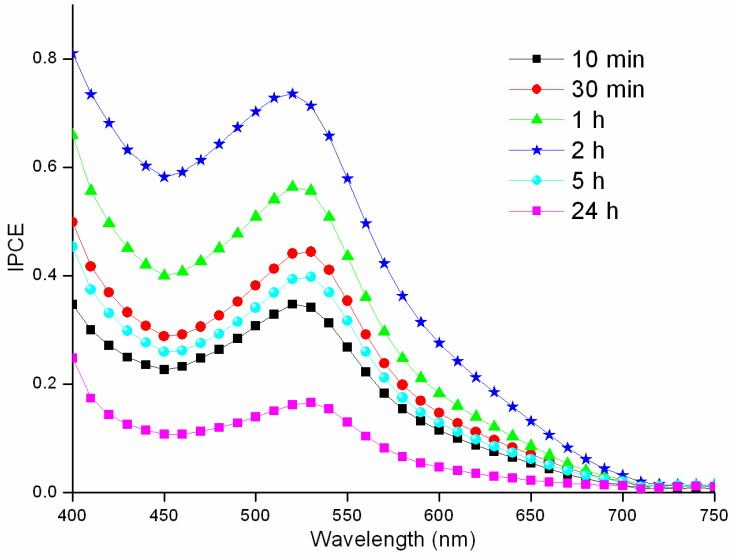

Figure 6.11: IPCE curves of sponge-like ZnO-based DSCs for different impregnation times in dye solution; the thickness of the ZnO layer is 5 μm.

Since the long-term formation of Zn^{2+}/dye aggregates is expected to be partially suppressed when a more basic dye solution is used [127], the effect of pH of the sensitizing mixture was experimentally evaluated adding 0.2 mM sodium hydroxide to the N719 solution. The pH was thus changed from 6.5 (normal solution) to 9 (hydroxide containing solution). The 5 μm ZnO sample incubated on the basic solution for 24 h showed an overall efficiency of 2.56%, significantly higher than the corresponding value (1.90%) obtained with a dipping in the slightly acid solution for the same time interval (see Fig. 6.12 and Table 6.4). The deprotonation of the solution reduces the kinetics of Zn^{2+} ion release, allowing longer sensitization by suppressing the formation of aggregates. The degradation mechanism of the ZnO layer brings to an increase of the charge recombination phenomenon, but this effect can be reduced while sensitizing the photoelectrode in the basic solution. This feature is evident by comparing the phase plots derived from EIS measurement presented in Fig. 6.13: the rate constant for recombination of the sample subjected to 24 h of incubation in normal solution (613 s^{-1}) is higher with respect to the sample sensitized in the basic mixture (420 s^{-1}). Thus, for an efficient long dye-sensitization process of ZnO electrodes, dyes with no acidic protons are preferred in order to suppress the dissolution of Zn surface ions and formation of Zn^{2+}/dye aggregates. These experimental evidences are in agreement with the arguments already proposed in literature [29]. For shorter incubation times, the same beneficial effect is not evidenced because the de-aggregation effect conflicts with the dye desorption that usually occurs in basic environments.

With the aim of exposing higher surface area to dye absorption in order to further increase the conversion efficiency, the ZnO thickness was varied from 5 to 15 μm by means of appropriate choice of the sputtering deposition time. In the thicker films, an increase of the photogenerated charges injected in the conduction band of the oxide is clearly observable, leading to better cell performances (Fig. 6.14). In fact, thicker photoelectrodes are able to load a higher amount of dye, thus allowing the injection of a higher number of carriers in the conduction band of the semiconductor, and the charge transport is efficient enough to allow the collection of the electrons at the FTO substrate. With the use of the thicker film (15 μm) and the optimal incubation time of 2 h, the highest value in solar energy conversion efficiency (4.94%) was obtained, as presented in Table 6.5. Interestingly, the recombination kinetics shows a dependence on the photoanode thickness. In particular, by looking at the Bode plots reported in Fig. 6.15, a shift of the phase peak towards lower frequencies can be observed while increasing the ZnO thickness. The evaluated rate constants for recombination at cell V_{oc} were equal to 266 s^{-1}, 83 s^{-1} and 21 s^{-1} for the 8 μm, 12.5 μm and 15 μm thick ZnO photoanodes, respectively. The dependence of the recombination on the photoanode thickness is probably related to the contribution of the back transfer of electrons at the FTO/electrolyte interface [133]. For thicker photoanodes, this parasitic effect loses importance, giving as a macroscopic result a higher overall carrier lifetime, as reported previously for mesoporous TiO_2 films [134].

Solution pH	J_{sc} (mA/cm^2)	V_{oc} (V)	FF	PCE (%)	ω_n (s^{-1})
6.5	5.87	0.67	0.48	1.90	613
9	7.66	0.58	0.58	2.56	420

Table 6.4: Photovoltaic performances of sponge-like ZnO-based DSCs for different pH of the sensitizing solution evaluated from I-V characterization and EIS analysis; the thickness of the ZnO layer is 5 μm, and the impregnation time is 24 h.

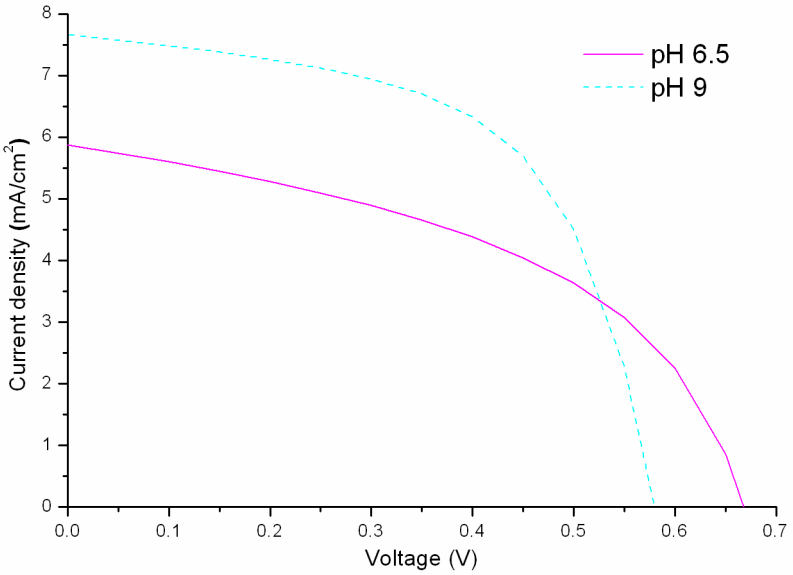

Figure 6.12: Current density-voltage curves of sponge-like ZnO-based DSCs for different pH of the sensitizing solution; the thickness of the ZnO layer is 5 μm, and the impregnation time is 24 h.

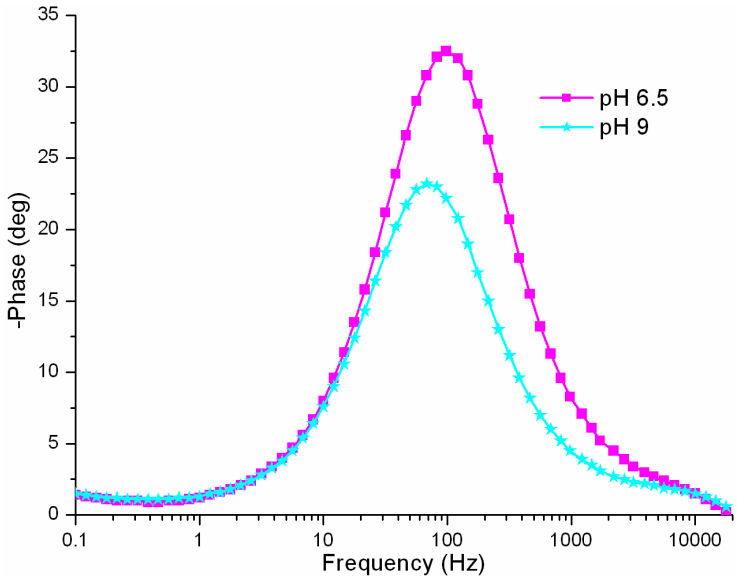

Figure 6.13: Bode plot of phase impedance of sponge-like ZnO-based DSCs for different pH of the sensitizing solution measured at cell V_{oc}; the thickness of the ZnO layer is 5 μm, and the impregnation time is 24 h.

ZnO thickness (μm)	J_{sc} (mA/cm^2)	V_{oc} (V)	FF	PCE (%)	ω_n (s^{-1})
5	8.95	0.62	0.57	3.09	322
8	11.12	0.61	0.53	3.59	266
12.5	13.44	0.60	0.54	4.58	83
15	14.44	0.57	0.60	4.94	21

Table 6.5: Photovoltaic performances of sponge-like ZnO-based DSCs for different thickness of the ZnO layer evaluated from I-V characterization and EIS analysis; the impregnation time is 2 h.

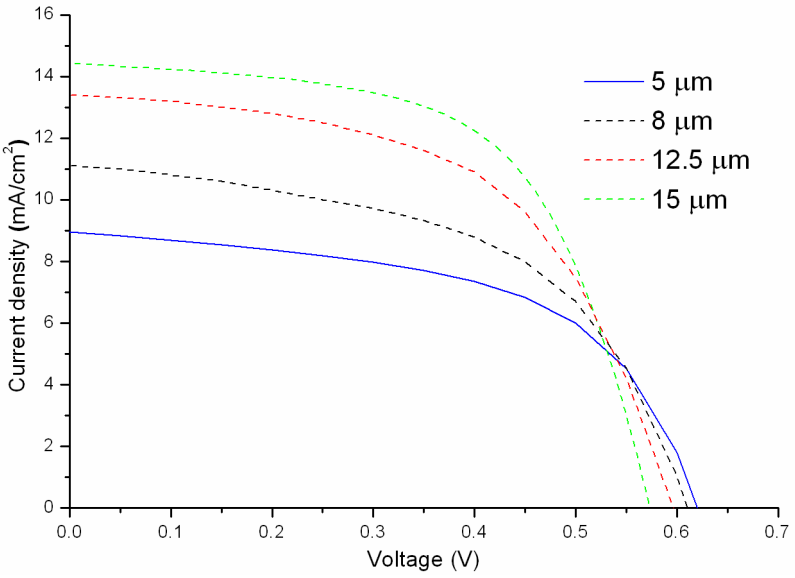

Figure 6.14: Current density-voltage curves of sponge-like ZnO-based DSCs for different thickness of the ZnO layer; the impregnation time is 2 h.

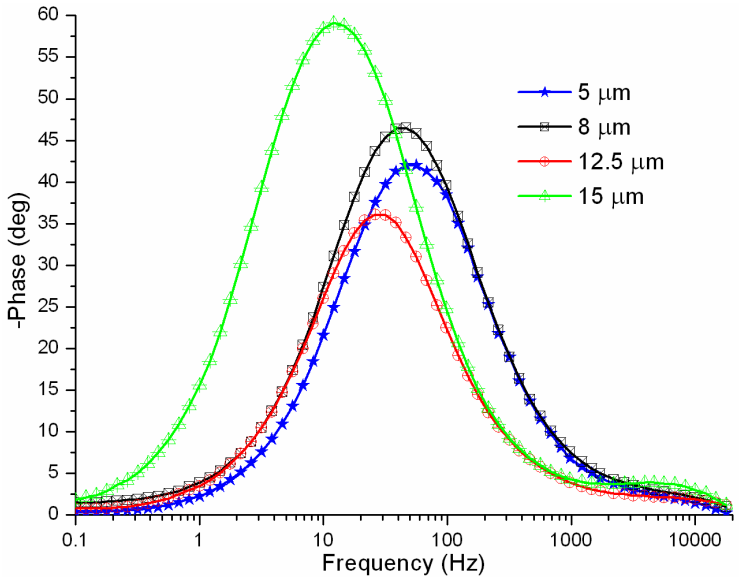

Figure 6.15: Bode plot of phase impedance of sponge-like ZnO-based DSCs for different thickness of the ZnO layer measured at cell V_{oc}; the impregnation time is 2 h.

6.4 Anodic TiO_2 nanotube membranes

As introduced in Section 2.1.2, with the aim of improving the charge transport and minimizing the recombination mechanisms, different dimensionally confined materials such as nanowires, nanorods and nanotubes have been proposed as a promising alternative to randomly interconnected nanoparticles for photoanode fabrication in DSCs. In particular, anodized titanium oxide nanotube arrays, firstly proposed in 1999 [135], stand out for a faster and more efficient electron transport with respect to traditional NP-based photoanodes [35]. These NTs can be simply grown by the electrochemical oxidation of a Ti foil. The huge inconvenient is that the best working configuration of DSCs is based on a front-side illumination (to avoid light reflection at the cathode and absorption by the electrolyte) and so transparent electrodes are needed [35]. To overcome this problem, a possible solution consists in the growth of a thick TiO_2 NT array on Ti foil and its detachment and subsequent bonding onto the transparent conductive substrate employing a bonding interlayer [136]. During the detachment from the growth substrate, the characteristic blocking layer usually present between the bottom of the NTs and the Ti foil is removed [37], resulting in a further improvement of charge transport. The adhesion layer can be obtained by employing a TiO_2 sol, with appropriate thermal treatments and applied pressure.

In this section the photovoltaic performances and the electron transport properties of transparent TiO_2 NT-based DSCs will be presented. NT arrays with different lengths were fabricated by anodic oxidation of Ti foil and free-standing NT membranes were detached by the bulk metal and bonded on the FTO surface implementing a simple technological approach. The morphology and the crystal orientation of the TiO_2 NTs were investigated by different techniques. DSCs were assembled employing the microfluidic housing system, and the photovoltaic performance dependence on tube length and the effect of a $TiCl_4$ treatment were characterized by I-V, IPCE, OCVD and EIS measurements. The EIS data were fitted by TLM equivalent circuit in order to obtain information on the electron diffusion properties into the NTs, and the results were compared to NP-based photoanode in order to investigate the effect of the 1D pathway for charge collection.

6.4.1 Fabrication and characterization of the nanotube membranes

The growth mechanism of TiO_2 NT arrays in fluoride-based electrolyte can be described as the occurrence of three competitive reactions [137]: the field-assisted oxidation of Ti and the dissolution of Ti ions in the electrolyte are the first two processes, while the third is the chemical dissolution of Ti and TiO_2 through the etching due to fluoride ions. After the anodization of the Ti foil, a hexagonal close-packed TiO_2 nanotube array was successfully obtained. Free-standing NT membranes were then separated by the metallic substrate following a self-detaching procedure described in Section 6.4.2.

The final appearance of the TiO_2 NT array, before and after detachment, is shown in Figs. 6.16a and 6.16b. For an anodization time of 2 hours, a 12 μm-thick TiO_2 NT membrane was obtained (Fig. 6.16c), while for 3 and 4 hours the membrane thicknesses were 22 and 30 μm, respectively. The walls of the tubes are quite smooth (Fig. 6.16d) thanks to the polar organic nature of the electrolytic solution [138]. The average external diameter of the tubes was 120 nm. Figs.

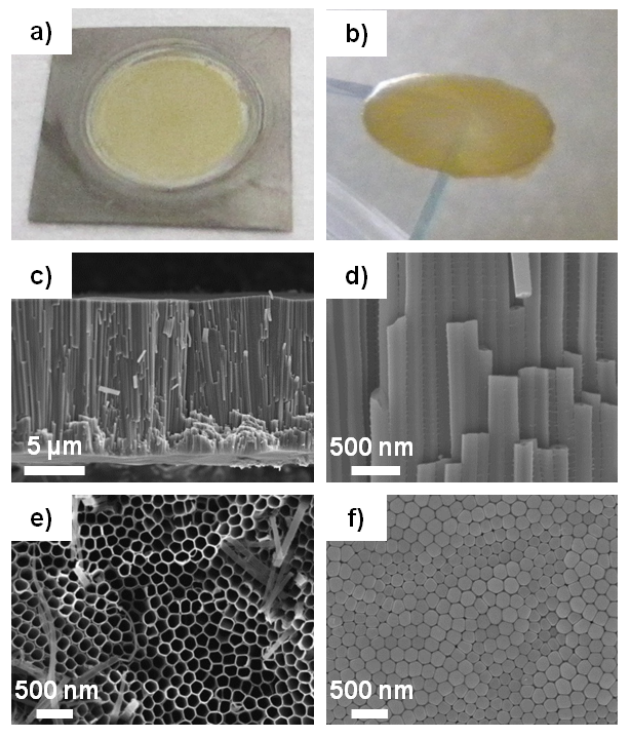

Figure 6.16: Photograph of as-anodized Ti foil (a) and self-standing membrane of TiO_2 NTs (b); FESEM micrographs showing the cross-section of TiO_2 NT array at different magnification (c, d); the top (e) and bottom (f) views of TiO_2 NTs.

6.16e and 6.16f show the top and the bottom of the NT membrane, revealing the hexagonally-packed assembly typical of the anodized titanium oxide.

Fig. 6.17 shows the XRD patterns of the as-grown and annealed TiO_2 NT array. It is possible to see that the former is completely amorphous while the latter presents peaks in perfect agreement with the reference patterns for titania anatase (JCPDS 89-4921), both in peak positions and relative intensities.

6.4.2 Photoanode fabrication

The process flow for the fabrication of a transparent photoanodes consists in the following steps. After anodization, free-standing NT membranes were easily separated by the metallic substrate without any crack following a self-detaching procedure consisting in repeated rinsing in DI-water and ethanol. The membranes were then transferred and bonded onto FTO-covered glass substrates employing a 4 μL drop of TiO_2 sol as a binder and applying a slight pressure with a N_2 flow. Finally, an annealing treatment was made to sinter the TiO_2 NPs of the sol and crystallize the nanotubes array. This approach for membrane detachment and bonding is easier than other previously reported in the literature [137] since it does not involve any chemical etching or mechanical splitting for membrane separation and only one thermal process is required both for membrane crystallization and attachment.

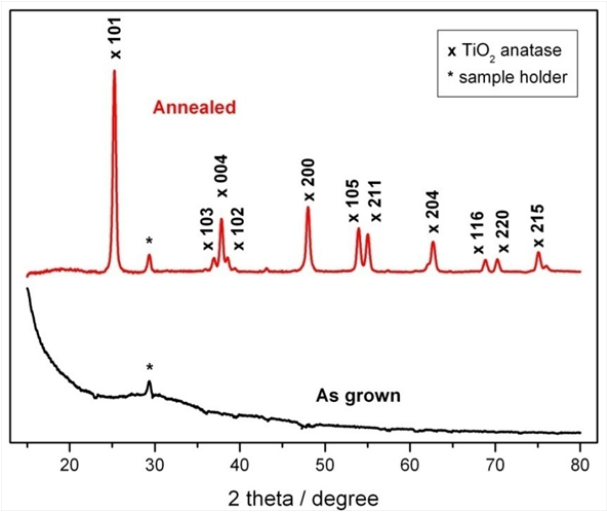

Figure 6.17: X-ray diffraction pattern of as-grown and annealed TiO_2 NT array.

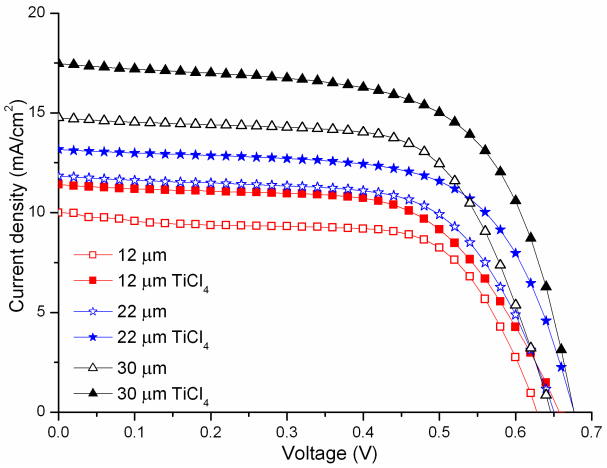

Figure 6.18: Current density-voltage curves of TiO_2 NT-based DSCs with and without $TiCl_4$ treatment for different nanotube lengths.

6.4.3 Evaluation of photovoltaic performances and transport properties

In Fig. 6.18 the results of I-V measurements performed on the cells fabricated using the NT array membranes are reported; in particular, the results obtained for the three different nanotube lengths (12, 22 and 30 μm), with and without the $TiCl_4$ treatment are shown. The relative photovoltaic parameters are reported in Table 6.6. By looking at these values, it can be noticed an increase of the photocurrent density while increasing the nanotube thickness: from 10.07 to 14.77 mA/cm^2 passing from 12 to 30 μm. This improvement has to be attributed to the increase of the total surface available for the dye anchoring. Moreover the $TiCl_4$ treatment led to a further improvement of the photovoltaic performances for all the samples under study. In fact, as introduced in Section 4.1.1, a downward shift of the TiO_2 conduction band occurs due to the effect of this treatment, resulting in an enhancement of the electron injection efficiency. Moreover a higher number of charge separation interfaces is originated, leading to an intensified light absorption [139]. The

Cell	J_{sc} (mA/cm^2)	V_{oc} (V)	FF	PCE (%)
12 μm	10.07	0.628	0.66	3.64
12 μm $TiCl_4$	11.41	0.657	0.62	4.65
22 μm	11.84	0.651	0.64	4.97
22 μm $TiCl_4$	13.17	0.677	0.65	5.82
30 μm	14.77	0.646	0.66	6.26
30 μm $TiCl_4$	17.47	0.677	0.64	7.56

Table 6.6: Photovoltaic parameters of TiO_2 NT-based DSCs with and without $TiCl_4$ treatment for different nanotube lengths.

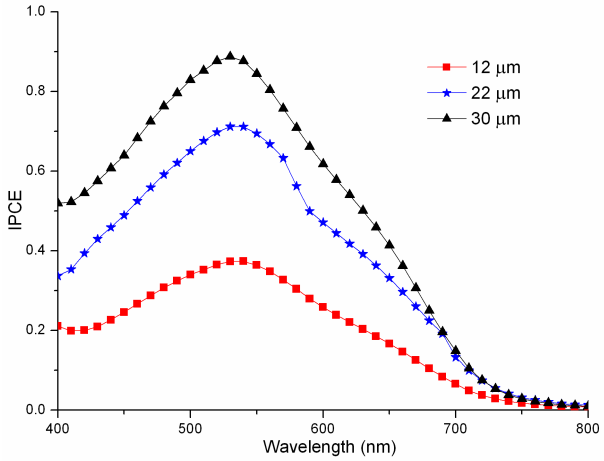

Figure 6.19: Incident photon-to-electron conversion efficiency spectra of $TiCl_4$-treated NT-based DSCs for different nanotube lengths.

overall effect is an increase of the J_{sc} values, and consequently of the photoconversion efficiency. A maximum PCE value of 7.56% has been obtained for the cell fabricated with 30 μm-thick nanotube membrane treated with $TiCl_4$.

The observed increase of short circuit current density while increasing the nanotube length was also confirmed by IPCE measurements, reported in Fig. 6.19 for the $TiCl_4$-treated cells. The spectra show an upward shift in the wavelength range from 400 to 750 nm, with a maximum IPCE value of 0.89 measured at 530 nm for 30 μm-length nanotubes.

The effect of the NT length on the recombination kinetics in the fabricated devices was studied through open circuit voltage decay measurements, whose results are reported in Fig. 6.20. No difference in the exponential decay was observed for the different NT membrane thickness, meaning that the electron lifetime is not dependent on nanotube length. A slower decay of the photovoltage (meaning an increase of the charge lifetime) was instead observed for the $TiCl_4$-treated cells (as shown in the inset of Fig. 6.20): this is an evidence of a reduced recombination rate due to the nanoparticle coverage on the nanotube walls that acts as a barrier for the interfacial recombination [109]. In fact, as reported in literature [140], the NPs could occupy nanotube surface impurities, defects and grain boundaries (that are the sites on which the recombination processes mainly occur).

In order to study in detail the recombination and transport properties of the NT membranes,

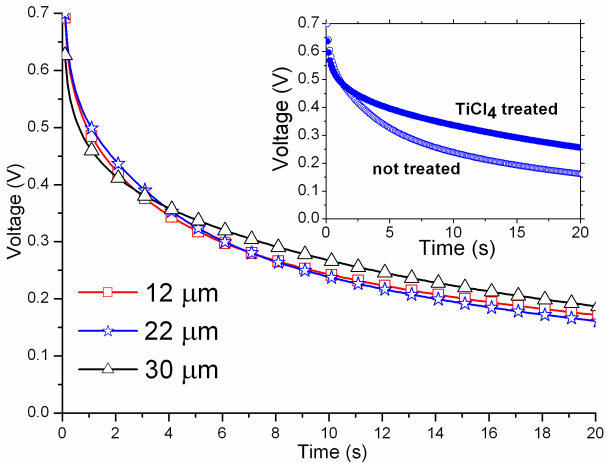

Figure 6.20: Open circuit voltage decay curves of not-treated NT-based DSCs for different nanotube lengths. In the inset the comparison between the cells fabricated with 22 μm thick NT membranes with and without $TiCl_4$ treatment is reported.

electrochemical impedance spectroscopy analysis was performed. From the equivalent circuit fitting of the experimental curves (exploiting the circuit reported in Fig. 3.5), the effective electron lifetime τ_n and the diffusion length L_n values were extracted and the results are reported in Fig. 6.21. The same parameters have been evaluated for a cell fabricated with a 8 μm-thick $TiCl_4$-treated layer of TiO_2 NPs (also shown in Fig. 6.21). As already observed from the OCVD measurements, it is evident an increase of the carrier lifetime in the NT-based DSCs due to the $TiCl_4$ treatment, while comparable values were obtained for the diffusion length, meaning that the charge transport properties of the NTs are adequate for electron collection even without the treatment [109]. A significant increase of both electron lifetime and diffusion length values was observed for the NT-based cells with respect to the NP-based one. In fact the number of surface states is proportional to specific area and the NT surface is a order of magnitude lower with respect to the NP one. For this reason the NT array presents a reduced number of defects and trap sites (such as grain boundaries) with respect to the NP layer, and the charge recombination rate is subsequently greatly reduced [141]. Moreover, thanks to the 1D structure, the charge transport is improved in the NT-based DSCs, while in the NP-based ones the transport mechanisms result more complicated due to a longer pathway for the electrons in the nanoparticle network. The improved transport properties of the NT-based cell are also confirmed by the diffusion coefficient values D_n, calculated through the Eq. 3.12: at cell open circuit voltage, the values of $4 \cdot 10^{-4}$ cm^2/s, $3 \cdot 10^{-4}$ cm^2/s and $0.8 \cdot 10^{-4}$ cm^2/s were found for the NT treated cell, NT untreated cell and NP cell, respectively.

6.5 Non-destructive analysis of DSC components

As introduced in Section 1.2.1, one of major issues of DSCs is their limited long-term stability over time, which up to now reached 20000 h under continued irradiance [142]. In order to further extend the stability, the understanding of the causes of degradation of the different cell components is

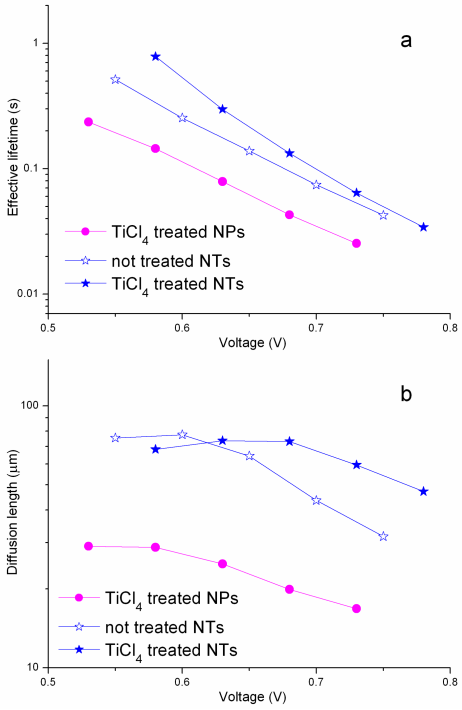

Figure 6.21: (a) Effective electron lifetime and (b) diffusion length dependence on the bias voltage for the cells fabricated with 22 μm-thick NT membranes with and without $TiCl_4$ treatment. For comparison, the same parameters extracted for a cell fabricated with 8 μm of $TiCl_4$- treated TiO_2 nanoparticles are reported.

essential. Many degradation phenomena, related to the different components, have been reported: bleaching of iodine due to UV illumination [143] or to water impurities in the electrolyte solution [144], Pt dissolution from the counter electrode caused by the electrolyte [145], dye degradation or desorption caused by UV irradiation, high temperature and presence of water [146, 147, 148], and changes in TiO_2 film structure [149]. However, an analysis of the components aimed at the identification of one or more phenomena among those listed above is up to now difficult to be performed without compromising the integrity of the cell, since the structure has to be definitely disassembled (due to the presence of the sealant exploited to avoid electrolyte leakages and protect the cell elements from the environment) in order to inspect its parts. An attempt to overcome this limitation was made [144] using scanning microscopy for semiconductor characterization, in which a point-by-point laser-induced photocurrent is measured and related to the presence of defects or to degradation phenomena. However the determination of which degradation process causes those defects and on which of the cell components it occurs is not straightforward.

In this framework, thanks to its reversible assembly and disassembly procedure, the microfluidic architecture could give a fundamental help. In this section, a study aimed to demonstrate that the microfluidic DSC is an effective investigation tool for the analysis of the different cell elements will be presented. By using this structure, an accelerated degradation in the cell was induced (see Section 4.1.5), and the behavior of the electrodes over time (for a period of three weeks) was monitored. In particular, the Pt-covered counter electrodes were analyzed through field emis-

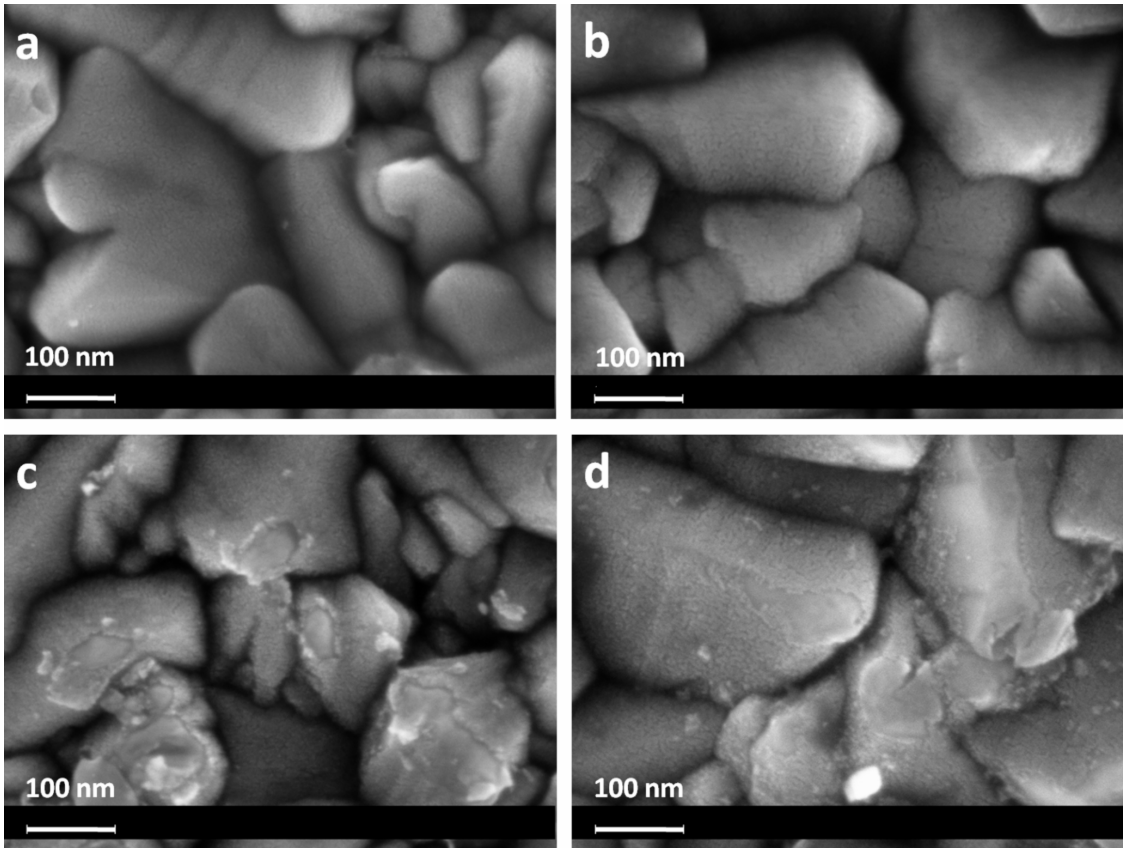

Figure 6.22: FESEM micrographs showing the top view of Pt-covered counter electrode of the freshly assembled cell (a), after one week (b), after two weeks (c) and after three weeks (d).

sion scanning electron microscopy, contact angle measurements and UV-visible spectroscopy; the photoanodes through UV-visible spectroscopy; the whole cells through current-voltage and electrochemical impedance spectroscopy measurements. Six cells were fabricated and analyzed within a period of three weeks: five cells were analyzed in all their components once a week, while the other cell was used as reference (it was not opened for all the investigation period and only the I-V measurement was performed once a week) in order to prove that the procedures of cell assembling and disassembling did not introduce modification of the components of the cell itself. Before performing the measurements on the different components, the electrolyte was removed and only then the cells were opened. After the measurements the cells were re-assembled and filled with the electrolyte. All the cells were kept in dark conditions when not being used.

6.5.1 Counter electrode investigation

Fig. 6.22 reports the FESEM micrographs of the Pt-covered counter electrodes for different ageing periods with the same magnification. A strong degradation on the Pt thin film after two weeks of operation can be clearly seen. In fact, after two weeks the Pt thin film is not continuous anymore and it peels off from some FTO grains. This effect was evidenced in all the samples analyzed.

Results of CA measurements show a strong variation of wetting properties of the FTO/Pt

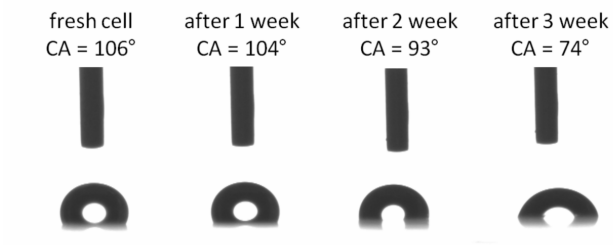

Figure 6.23: Contact angle images of DI water on Pt-covered counter electrode of the freshly assembled cell and after one, two and three weeks.

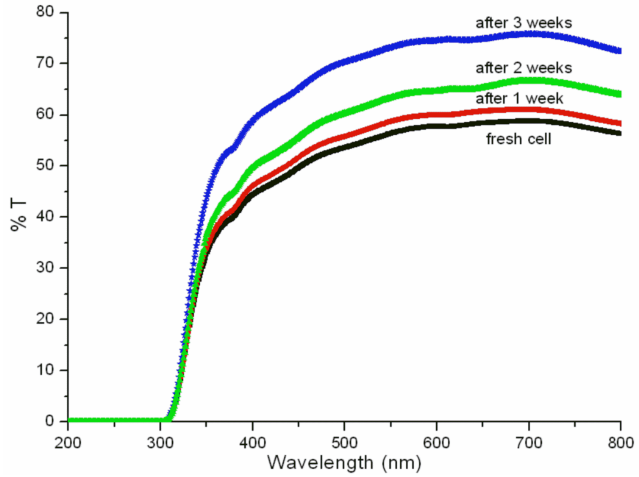

Figure 6.24: UV-visible transmittance spectra of Pt-covered counter electrodes.

counter electrode. The water CA values decrease over time from around 106° of the fresh cell to 74° of the third week (as reported in Fig. 6.23). This behavior is almost the same for all the cells under investigation and can be associated with the Pt layer degradation on the FTO as described by FESEM analysis.

UV-visible transmittance measurements performed on the counter electrodes are shown in Fig. 6.24. The results remain substantially unchanged till the first week, while an overall increase of the spectra is clearly observable starting from the second week. After three weeks the initial visible transmittance, whose value at 680 nm is 59% (due to the presence of the Pt layer which strongly reduces the visible transmittance of the FTO/glass, which is about 80%) increases to 76% for all the examined cells. This variation can be attributed to the dissolution of the Pt layer, and in fact this phenomenon, together with the formation of compounds of Pt with the iodide at the electrode surface, has already been reported [145]. From all the above results an aggressive effect of the electrolyte on the Pt thin film can be deduced.

6.5.2 Photoanode investigation

The absorbance spectra of the photoanodes are reported in Fig. 6.25. Clear differences are present between the fresh photoanode spectrum and the ones subsequently obtained after the first week:

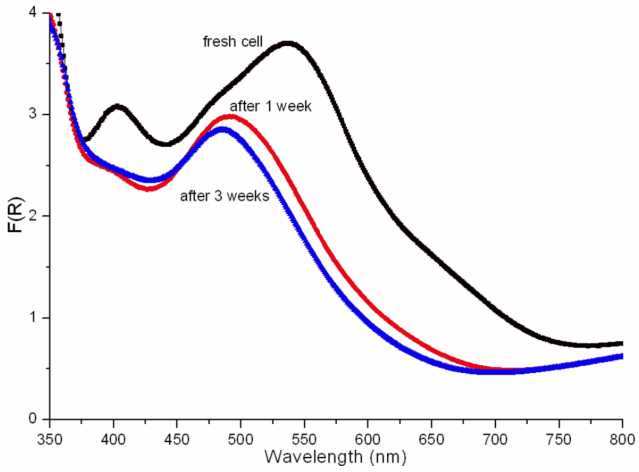

Figure 6.25: UV-visible absorbance spectra of dye-sensitized photoanodes.

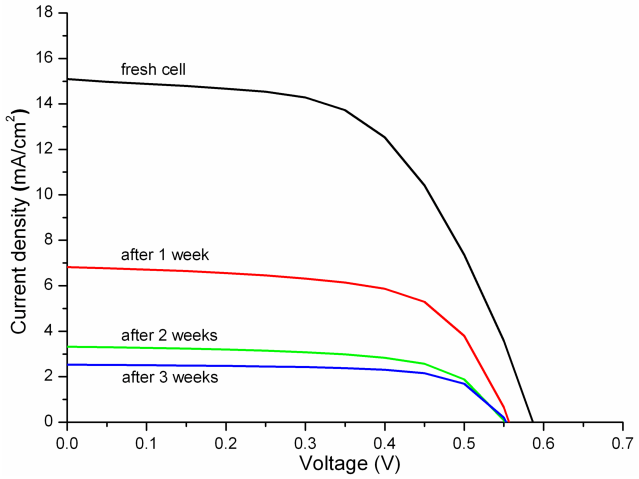

Figure 6.26: Current density-voltage curves of one of the fabricated cells.

in particular an overall decrease of the absorbance and the disappearance of the typical N719 dye peaks. These effects evidence noticeable dye degradation since the first week. The subject has been largely investigated in the literature: the N719 degradation has been attributed to the interaction with the electrolyte, to water and air contamination and to exposure to UV light and temperatures higher than 135 °C [146]. The thiocyanate ion ligand (SCN^-) has been identified to be the most sensitive part of the N719 dye: it was found to be substituted with H_2O/OH^- and also with triiodide ions, leading to a substantial instability of the dye in presence of air and water. Furthermore, the electrochemical oxidation of the N719 complex adsorbed on a TiO_2/FTO film has been reported to give rise to new weaker absorption bands at about 470 and 645 nm [150].

6.5.3 Complete cell investigation

The above results obtained for both the photoanode and the counter electrode were successfully confirmed by the electrical characterization. An example of current density-voltage curves of the cells is shown in Fig. 6.26 while the average photovoltaic parameters (mean values for the five

Cell	J_{sc} (mA/cm^2)	V_{oc} (V)	FF	PCE (%)	R_{CE} (Ω)	τ_n (ms)	Ref. cell PCE (%)
Fresh	15.04	0.60	0.57	5.08	2.87	10.90	5.01
After 1 week	6.80	0.56	0.63	2.39	3.49	5.83	2.38
After 2 weeks	3.53	0.55	0.63	1.22	9.11	4.95	1.16
After 3 weeks	2.59	0.55	0.68	0.96	9.49	4.49	0.97

Table 6.7: Average cell parameters (mean values for five cells) evaluated from I-V characterization and EIS analysis. The last column reports the photoconversion efficiency (PCE) values for the reference cell.

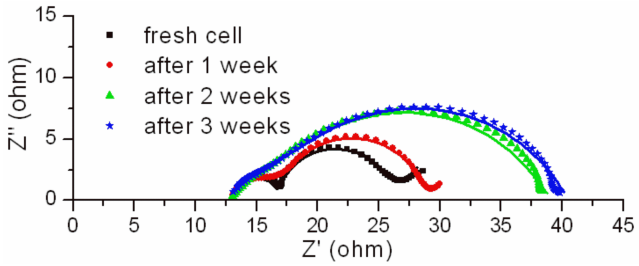

Figure 6.27: Electrochemical impedance spectra of one of the fabricated cells (the points are experimental data while the continuous lines are fitting curves).

cells) are summarized in Table 6.7. There a strong decrease of the total conversion efficiency can be noticed just after one week (quite halved with respect to the fresh cell), due to the decrease of both J_{sc} and V_{oc}. Going on with time, the current density keeps decreasing due to depletion of the dye and its detachment from the photoanode [147, 148], while the decrease of the open circuit voltage is less pronounced. Such a decrease has already been attributed to a positive shift of the TiO_2 conduction band caused by water [151].

The impedance spectra of a representative cell for every condition are reported in Fig. 6.27. From the spectra it is possible to observe that after one week the degradation of the photoanode occurs (the central arc height and width both increased). After two weeks also the contribution of the counter electrode becomes evident (the high-frequency arc almost disappears). The shape of the curve changes from quasi-circular to a Gerisher type (see Section 3.5.1): in this condition the diffusion length is lower than the TiO_2 thickness, implying a strong recombination rate (recombination occurs before the electrons arrive at the substrate). The experimental curves were fitted by using the circuit depicted in Fig. 3.6. By looking at the fitting values reported in Table 6.7, is it possible to observe that R_{CE} values starts increasing from week two. In fact, the Pt thin film peeling off from the electrode surface makes the collection of charges become poor and the corresponding value of the resistance increase. Moreover the platinum, diffusing to the photoanode, could act as a recombination site (so causing a further increase of the recombination rate). On the basis of the EIS results it is also possible to relate the influence of the photoanode degradation on the decrease of the open circuit voltage [152]. The electron lifetime values were calculated using the Eq. 3.11, and these values also are reported in Table 6.7. There is a direct relation between the decrease of the lifetime, due to an increase of recombination caused by the photoanode degradation, and V_{oc}.

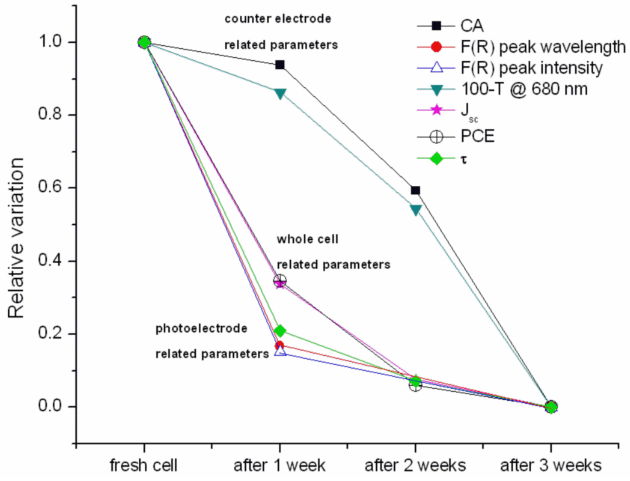

Figure 6.28: Behavior of cell parameters related to the different components: CA and transmittance values for the counter electrode; electron lifetime, position and intensity of the dye absorbance peak for the photoanode; current density and photoconversion efficiency for the whole cell. All the points are normalized using the formula $(x\text{-}x_{min})/(x_{max}\text{-}x_{min})$, where x_{min} and x_{max} are the minimum and the maximum values of the analyzed parameter x.

In order to summarize all the results obtained from the different characterizations, in Fig. 6.28 the behaviors of cell parameters related to the different components are reported. The following parameters were chosen in order to monitor the degradation over time: CA and transmittance values (measured at the wavelength of 680 nm) for the counter electrode; electron lifetime, position and intensity of the dye absorbance peak (the one centered at about 534 nm in the fresh cell spectrum) for the photoanode; current density and photoconversion efficiency for the whole cell. From the analysis of this graph it is clearly visible that the parameters related to the photoanode experience a decrease in the first week, while the counter electrode ones are quite constant in that period. During the second week a decrease is evident also for CA and transmittance values, proving that degradation has occurred at the Pt-covered electrode.

Finally, the results of the I-V characterization on the reference cell (reported only in terms of conversion efficiencies in the last column of Table 6.7) show no difference with respect to the cells that were opened and closed during the whole period of analysis. The efficiency values of the reference cell are in fact in good agreement with those related to the other cells, proving that no additional degradation was caused to the cells by the assembling and disassembling procedures. All the results proved the effectiveness of the microfluidic architecture as a test tool in the study of the degradation phenomena in DSCs.

6.6 Conclusions

In this chapter some applications of the innovative microfluidic architecture for DSC were reported.

The first one was the test of different innovative organic sensitizers, with interesting results in terms of photovoltaic conversion efficiencies obtained employing them in microfluidic devices.

The study was then focused on the novel hemi-squaraine organic dye, whose squarate moiety was found to strongly interacts with the anatase surface, giving rise to an optimal alignment of the electronic molecular levels with respect to the oxide energy bands, thus favoring adiabatic electron transfer from the excited molecule to the semiconductor. This results in an efficient electron injection with an observed maximum IPCE of 87%, and efficiency equal to 3.54%.

The microfluidic architecture was successfully employed for the fabrication and characterization of DSCs made with coral-shaped ZnO photoanodes. A simple and scalable method for the synthesis of sponge-like Zn structure was presented. The Zn nanostructures were oxidized with a simple thermal treatment in air, obtaining a porous ZnO film with a 3D coral-like morphology. The solar energy conversion efficiency of DSCs based on ZnO films sensitized with Ru-based dyes was evaluated. The sensitization procedure was refined, being the optimal sensitization time equal to 2 hours. Using a 15 μm-thick photoanode, a noticeable photovoltaic conversion efficiency of 4.94% was evaluated, with a charge carrier lifetime at open circuit voltage equal to 48 ms.

Another application of the microfluidic DSC was the study of the photovoltaic performances and transport properties of anodically grown TiO_2 nanotube membranes employed as transparent DSC photoanodes. The cell performances and the electron transport properties dependence on $TiCl_4$ treatment and tube length were characterized and a maximum value for the PCE equal to 7.56% was obtained for the cell fabricated with a 30 μm-thick nanotube membrane treated with $TiCl_4$. Information on the electron diffusion properties into the NTs was obtained by equivalent circuit fitting of the EIS spectra. A significant increase of both electron lifetime and diffusion length values was observed for the NT-based cells with respect to a NP-based one.

Finally, a study aiming to prove that the innovative microfluidic housing system described in this work is effective as an investigation tool for the analysis of the constituent materials of dye-sensitized solar cells was reported. The reversible sealing of such structure allowed characterizing in a non-destructive way the cell components periodically over three weeks and linking the decrease of the total photovoltaic conversion efficiency to the different cell elements. In particular, the Pt-covered counter electrode was subjected to degradation after two weeks mainly caused by the chemical interaction with the electrolyte. For what concerns the photoanode, instead, a degradation of the dye after just one week (due to the contact with electrolyte and air) was evidenced. The results showed how it was possible to perform a degradation analysis over time by exploiting the microfluidic architecture, which is the only laboratory prototype proposed up to now that offers this possibility.

Chapter 7

Conclusions and future works

The goals of the thesis work were the design, the fabrication and the characterization of an innovative dye-sensitized solar cell architecture based on microfluidic concepts. By using such a structure, a large number (higher than 500) of small laboratory DSCs were fabricated with a high degree of assembly reproducibility; moreover different interesting applications were developed, namely the testing of some innovative materials like photoanodes and sensitizers, and the analysis of the cell components over time.

The first part of the work was focused on the design and fabrication of the microfluidic housing system for DSCs. This architecture is constituted by all the elements of a standard Grätzel's cell (photoanode, counter electrode and liquid electrolyte) in which the electrolyte solution is confined by means of a PDMS membrane; the closure is guaranteed by a PMMA clamping system, which allows the easy assembly and disassembly of the device. The sealing capability of the structure was studied with a dedicated fluidic set-up, and good sealing performances for a wide range of operating pressure and temperature were obtained. Moreover the novel architecture exhibited improved photovoltaic performances with respect to non-fluidic DSC.

The microfluidic architecture was then modified in order to solve some fabrication weak points. By using this structure, a study on fabrication reproducibility was carried out, in which optimal results were achieved (a standard deviation equal to 10% was obtained for the photoconversion efficiency values). The fabrication reproducibility will be further improved in the future through the use of a screen printing machine for the NP-based photoanode preparation, which will guarantee a higher uniformity of the TiO_2 layer. Moreover the effect of the membrane thickness was analyzed by varying this parameter in the range 100 – 200 μm and interesting conclusions were obtained from the EIS curves interpretation. However it has to be noted that, due to the difficulty of fabricating very thin PDMS membranes, the microfluidic assembly is not the best choice for studying electrolyte thickness values of 25 – 60 μm, which are normally adopted in non-fluidic devices. Finally the transmission line model was successfully applied to the EIS analysis of the

microfluidic architecture, and the obtained results were found to be in good agreement with the values reported in the literature for non-fluidic devices.

All the obtained results demonstrated the effectiveness of the microfluidic housing system as a prototype which can be used for laboratory tests on different DSC elements. Then, the second part of the work concerned the applications of the microfluidic architecture.

Different novel organic dyes were tested as sensitizers, with interesting results in terms of photovoltaic performances. The attention was then focused on one of these new dyes, the hemi-squaraine one; its photovoltaic performances were evaluated and an attempt of improvement was made by using chenodeoxycholic acid as co-adsorbent in order to reduce dye aggregation. Additional work needs to be done regarding this topic; in fact the photovoltaic performances of the hemi-squaraine-based DSC can be further improved by optimizing the sensitizing time and the CDCA concentration and, moreover, detailed studies on other sensitizers will be carried out. The microfluidic architecture presents the advantage of a quick assembly procedure and it can be exploited for the monitoring of the dye-impregnated photoanode properties before and after the usage of the cell. This housing system has demonstrated to be a very useful tool for the study of the in-cell behavior of organic dyes, also in the case of new dyes with not yet optimized time-stability.

Two different innovative materials were successfully employed as DSC photoanodes, namely the sponge-like ZnO and the anodic TiO_2 nanotubes. Both of them were characterized in terms of photovoltaic and charge transport properties, in particular examining their dependence on the oxide thickness. Moreover, only regarding the sponge-like ZnO, also the effect of the soaking time and of the sensitizing solution pH was studied; in fact, differently for what happens with TiO_2, Ru-based dyes can cause the long-term degradation to ZnO surface and the formation of Zn^{2+}/dye aggregates, leading to the decrease of cell performances. This study will be further carried on also considering the dye concentration, because all the three parameters can influence the equilibrium between the dye loading and the surface degradation. Moreover both the novel photoanode materials will be used in conjunction with quasi-solid or solid-state electrolytes thanks to their morphologies that can improve the electrolyte infiltration within the nanostructures.

The microfluidic architecture was successfully employed as investigation tool for the analysis of the constituent elements of dye-sensitized solar cells. This is in my opinion the most peculiar application of the microfluidic structure. Thanks to its capability of assembly and disassembly, an accelerated degradation was induced in the devices, and the behavior of the electrodes was successfully monitored for a period of three weeks. Even if problems related to the air penetration within the PDMS cannot be avoided, none of the available architectures for DSC laboratory prototypes offer the possibility of degradation analysis. The investigation of a not-accelerated degradation of different kind of counter electrode catalyst materials (evaporated Pt, thermally decomposed Pt and sputtered graphite) over time is currently under study, and in the future also other constituent materials could be analyzed.

Bibliography

[1] U. S. Energy Information Administration, International Energy Outlook 2011, September 2011, http://www.eia.gov/forecasts/ieo/index.cfm

[2] Intergovernmental Panel on Climate Change, http://www.ipcc.ch/index.htm

[3] European Parliament seals climate change package, http://www.europarl.europa.eu/sides/getDoc.do?pubRef=-//EP//TEXT+IM-PRESS+20081216IPR44857+0+DOC+XML+V0//EN

[4] M. Grätzel, "Photoelectrochemical cells", *Nature* **414** (2001) 338-344.

[5] http://org.ntnu.no/solarcells/pages/Chap.2.php

[6] http://webstore.iec.ch/Webstore/webstore.nsf/ArtNum_PK/37114, http://webstore.iec.ch/webstore/webstore.nsf/Artnum_PK/39336

[7] J. Nelson, "The physics of solar cells", (2003) Imperial College Press, London.

[8] http://www.eyesolarlux.com/Solar-simulation-energy.htm

[9] http://www.keithley.com/solar_cell

[10] A. Sacco, L. Rolle, L. Scaltrito, E. Tresso and C. F. Pirri, "Characterization of photovoltaic modules for low-power indoor application", *Appl. Energy* **102** (2013) 1295-1302.

[11] http://www.astro.caltech.edu/observatories/palomar/lfc/Si-002_qe.gif

[12] D. M. Chapin, C. S. Fuller and G. L. Pearson, "A new silicon p-n junction photocell for converting solar radiation into electrical power", *J. Appl. Phys.* **25** (1954) 676-677.

[13] S. M. Sze and K . K. Ng, "Physics of semiconductor devices", (2007) John Wiley & Sons, Hoboken.

[14] K. Kato, A. Murata and K. Sakuta, "Energy Payback Time and Life-Cycle CO_2 Emission of Residential PV Power System with Silicon PV Module", Appendix B-8. Environmental Aspects of PV Power Systems (1997) Utrecht University, Report Number 97072.

[15] S. J. Fonash, "Solar cell devices physics", (2010) Academic Press, Oxford.

[16] M. Pagliaro, G. Palmisano and R. Ciriminna, "Il nuovo fotovoltaico", (2008) Dario Flaccovio Editore, Palermo.

[17] W. Shockley and H. J. Queisser, "Detailed balance limit of efficiency of p-n junction solar cells", *J. Appl. Phys.* **32** (1961) 510.

[18] S. E. Shaheen, C. J. Brabec, N. S. Sariciftci, F. Padinger, T. Fromherz and J. C. Hummelen, "2.5% efficient organic plastic solar cells", *Appl. Phys. Lett.* **78** (2001) 841-843.

[19] B. O'Regan and M. Grätzel, "A low-cost, high-efficiency solar cell based on dye-sensitized colloidal TiO_2 films", *Nature* **353** (1991) 737-740.

[20] S. Ito, T. N. Murakami, P. Comte, P. Liska, C. Grätzel, M. K. Nazeeruddin and M. Grätzel, "Fabrication of thin film dye sensitized solar cells with solar to electric power conversion efficiency over 10%", *Thin Solid Films* **516** (2008) 4613-4619.

[21] NREL cell best efficiencies chart, http://www.nrel.gov/ncpv/images/efficiency_chart.jpg

[22] M. K. Nazeeruddin, E. Baranoff, and M. Grätzel, "Dye-sensitized solar cells: A brief overview", *Sol. Energy* **85** (2011) 1172-1178.

[23] M. Grätzel, "Solar energy conversion by dye-sensitized photovoltaic cells", *Inorg. Chem.* **44** (2005) 6841-6851.

[24] N. Vlachopoulos, P. Liska, J. Augustynski and M. Graetzel, "Very efficient visible light energy harvesting and conversion by spectral sensitization of high surface area polycrystalline titanium dioxide films", *J. Am. Chem. Soc.* **110** (1988) 1216-1220.

[25] http://www.aerosil.com/product/aerosil/en/industries/application-areas/dye-sensitized-solar-cells/pages/default.aspx

[26] M. Grätzel, "Perspectives for dye-sensitized nanocrystalline solar cells", *Prog. Photovolt. Res. Appl.* **8** (2000) 171-185.

[27] C. Sima, C. Grigoriu and S. Antohe, "Comparison of the dye-sensitized solar cells performances based on transparent conductive ITO and FTO", *Thin Solid Films* **519** (2010) 595-597.

[28] A. Hagfeldt, G. Boschloo, L. Sun, L. Kloo and H. Pettersson, "Dye-Sensitized Solar Cells", *Chem. Rev.* **110** (2010) 6595-6663.

[29] K. Keis, E. Magnusson, H. Lindström, S.-E. Lindquist and A. Hagfeldt, "A 5% efficient photoelectrochemical solar cell based on nanostructured ZnO electrodes", *Sol. Energ. Mat. Sol. C.* **73** (2002) 51-58.

[30] H. Zheng, Y. Tachibana and K. Kalantar-Zadeh, "Dye-sensitized solar cells based on WO_3", *Langmuir* **26** (2010) 19148-19152.

[31] J. Z. Ou, R. A. Rani, M.-H. Ham, M. R. Field, Y. Z., H. Zheng, P. Reece, S. Zhuiykov, S. Sriram, M. Bhaskaran, R. B. Kaner and K. Kalantar-zadeh, "Elevated temperature anodized Nb_2O_5: a photoanode material with exceptionally large photoconversion efficiencies", *ACS Nano* **6** (2012) 4045-4053.

[32] Q. He, Z. Zhang, J. Xiong, Y. Xiong and H. Xiao, "A novel biomaterial — Fe_3O_4:TiO_2core-shell nano particle with magnetic performance and high visible light photocatalytic activity", *Optical Materials* **31** (2008) 380-384.

[33] U. Diebold, "The surface science of titanium nanoxide", *Surf. Sci. Rep.* **48** (2003) 53-229.

[34] K. Fujihara, A. Kumar, R. Jose, S. Ramakrishna and S. Uchida, "Spray deposition of electrospun TiO_2 nanorods for dye-sensitized solar cell", *Nanotechnology* **18** (2007) 365709 (5 pp).

[35] G. K. Mor, O. K. Varghese, M. Paulose, K. Shankar and C. A. Grimes, "A review on highly ordered, vertically oriented TiO_2 nanotube arrays: Fabrication, material properties, and solar energy applications", *Sol. Energ. Mat. Sol. C.* **90** (2006) 2011-2075.

[36] X. Feng, K. Shankar, O. K. Varghese, M. Paulose, T. J. Latempa and C. A. Grimes, "Vertically aligned single crystal TiO_2 nanowire arrays grown directly on transparent conducting oxide coated glass: synthesis details and applications", *Nano Lett.* **8** (2008) 3781-3786.

[37] S. P. Albu, A. Ghicov, S. Aldabergenova, P. Drechsel, D. LeClere, G. E. Thompson, J. M. Macak and P. Schmuki, "Formation of double-walled TiO_2 nanotubes and robust anatase membranes", *Adv. Mater.* **20** (2008) 4135-4139.

[38] B. Liu and E. S. Aydil, "Growth of oriented single-crystalline rutile TiO_2 nanorods on transparent conducting substrates for dye-Sensitized solar cells", *J. Am. Chem. Soc.* **131** (2009) 3985-3990.

[39] Q. Zhang, C. S. Dandeneau, X. Zhou and G. Cao, "ZnO nanostructures for dye-sensitized solar cells" *Adv. Mater.* **21** (2009) 4087-4108.

[40] R. Jose, V. Thavasi and S. Ramakrishna, "Metal oxides for dye-sensitized solar cells", *J. Am. Ceram. Soc.* **92** (2009) 289-301.

[41] D. Calestani, M. Z. Zha, L. Zanotti, M. Villani and A. Zappettini, "Low temperature thermal evaporation growth of aligned ZnO nanorods on ZnO film: a growth mechanism promoted by Zn nanoclusters on polar surfaces", *CrystEngComm* **13** (2011) 1707-1712.

[42] Q. Li, V. Kumar, Y. Li, H. Zhang, T. J. Marks and R. P. H. Chang, "Fabrication of ZnO nanorods and nanotubes in aqueous solutions", *Chem. Mater.* **17** (2005) 1001-1006.

[43] J. H. Xiang, P. X. Zhu, Y. Masuda, M. Okuya, S. Kaneko and K. Koumoto, "Flexible solar-cell from zinc oxide nanocrystalline sheets self-assembled by an in-situ electrodeposition process", *J. Nanosci. Nanotechnol.* **6** (2006) 1797-1801.

[44] C.-H. Ku and J.-J. Wu, "Electron transport properties in ZnO nanowire array/nanoparticle composite dye-sensitized solar cells", *Appl. Phys. Lett.* **91** (2007) 093117-1.

[45] T. Hanmin, L. Lifei, L. Bin, Y. ShiKui, W. Xiangyan, W. Ying, Y. Tao and Z. Zhigang, "Influence of capacitance characteristic on dye-sensitized solar cell's IPCE measurement", *J. Phys. D Appl. Phys.* **42** (2009) 045109.

[46] A. Calzolari, A. Ruini and A. Catellani, "Anchor group versus conjugation: Ttoward the gap-state engineering of functionalized ZnO(1010) surface for optoelectronic applications", *J. Am. Chem. Soc.* **133** (2011) 5893-5899.

[47] F.-T. Kong, S.-Y. Dai and K.-J. Wang, "Review of recent progress in dye-sensitized solar cells", *Advances in OptoElectronics* **2007** (2007) Article ID 75384.

[48] A. Mishra, M. K. R. Fischer and P. Bäuerle, "Metal-free organic dyes for dye-sensitized solar cells: from structure: Property relationships to design rules", *Angew. Chem. Int. Edit.* **48** (2009) 2474-2499.

[49] G. Cicero, G. Musso, A. Lamberti, B. Camino, S. Bianco, D. Pugliese, F. Risplendi, A. Sacco, N. Shahzad, A. M. Ferrari, B. Ballarin, C. Barolo, E. Tresso and G. Caputo, "Combined experimental and theoretical investigation of the hemi-squaraine/TiO_2 interface for dye sensitized solar cells", *Phys. Chem. Chem. Phys.* in press (doi: 10.1039/C3CP50559F).

[50] M. K. Nazeeruddin, A. Kay, I. Rodicio, R. Humphrey-Baker, E. Muller, P. Liska, N. Vlachopoulos and M. Grätzel, "Conversion of light to electricity by cis-X_2bis(2,2'-bipyridyl-4,4'-dicarboxylate)ruthenium(II) charge-transfer sensitizers (X = Cl^-, Br^-, I^-, CN^-, and SCN^-) on nanocrystalline titanium dioxide electrodes", *J. Am. Chem. Soc.* **115** (1993) 6382-6390.

[51] M. K. Nazeeruddin , P. Péchy and M. Grätzel, "Efficient panchromatic sensitization of nanocrystalline TiO_2 films by a black dye based on atrithiocyanato-ruthenium complex", *Chem. Commun.* **18** (1997) 1705-1706.

[52] A. Jena, S. P. Mohanty, P. Kumar, J. Naduvath, V. Gondane, P. Lekha, J. Das, H. K. Narula, S. Mallick and P. Bhargava, "Dye Sensitized Solar Cells: A review", *Trans. Ind. Ceram. Soc.* **71** (2012) 1-16.

[53] G.-W. Lee, D. Kim, M. J. Ko, K. Kim and N.-G. Park, "Evaluation on over photocurrents measured from unmasked dye-sensitized solar cells", *Sol. Energy* **84** (2010) 418-425.

[54] K. Hara, K. Sayama, Y. Ohga, A. Shinpo, S. Suga and H. Arakawa, "A coumarin-derivative dye sensitized nanocrystalline TiO_2 solar cell having a high solar-energy conversion efficiency up to 5.6%", *Chem. Commun.* **6** (2001) 569-570.

[55] K. Hara, Z.-S. Wang, T. Sato, A. Furube, R. Katoh, H. Sugihara, Y. Dan-oh, C. Kasada, A. Shinpo and S. Suga, "Oligothiophene-containing coumarin dyes for efficient dye-sensitized solar cells", *J. Phys. Chem.* B **109** (2005) 15476-15482.

[56] T. Horiuchi, H. Miura and S. Uchida, "Highly-efficient metal-free organic dyes for dye-sensitized solar cells", *Chem. Commun.* **24** (2003) 3036-3037.

[57] S. Ito, H. Miura, S. Uchida, M. Takata, K. Sumioka, P. Liska, P. Comte, P. Pechy and M. Grätzel, "High-conversion-efficiency organic dye-sensitized solar cells with a novel indoline dye", *Chem. Commun.* **41** (2008) 5194-5196.

[58] X. Ma, J. Hua, W. Wu, Y. Jin, F. Meng and H. Tian, "A high-efficiency cyanine dye for dye-sensitized solar cells", *Tetrahedron* **64** (2008) 345-350.

[59] W. Wu, J. Hua, Y. Jin, W. Zhan and H. Tian, "Photovoltaic properties of three new cyanine dyes for dye-sensitized solar cells", *Photochem. Photobiol. Sci.* **7** (2008) 63-68.

[60] J.-H. Yum, P. Walter, S. Huber, D. Rentsch, T. Geiger, F. Nüesch, F. De Angelis, M. Grätzel and M. K. Nazeeruddin, "Efficient far red sensitization of nanocrystalline TiO_2 films by an unsymmetrical squaraine dye", *J. Am. Chem. Soc.* **129** (2007) 10320-10321.

[61] T. Geiger, S. Kuster, J.-H. Yum, S.-J. Moon, M. K. Nazeeruddin, M. Grätzel and F. Nüesch, "Molecular design of unsymmetrical squaraine dyes for high efficiency conversion of low energy photons into electrons using TiO_2 nanocrystalline films", *Adv. Funct. Mater.* **19** (2009) 2720-2727.

[62] J.-H. Yum, S.-R. Jang, P. Walter, T. Geiger, F. Nuesch, S. Kim, J. Ko, M. Grätzel and M. K. Nazeeruddin, "Efficient co-sensitization of nanocrystalline TiO_2 films by organic sensitizers", *Chem. Commun.* **44** (2007) 4680-4682.

[63] A. Hauch and A. Georg, "Diffusion in the electrolyte and charge-transfer reaction at the platinum electrode in dye-sensitized solar cells", *Electrochim. Acta* **46** (2001) 3457-3466.

[64] A. Lamberti, A. Sacco, S. Bianco, E. Giuri, M. Quaglio, A. Chiodoni and E. Tresso, "Microfluidic sealing and housing system for innovative dye-sensitized solar cell architecture", *Microelectron. Eng.* **88** (2011) 2308-2310.

[65] C. Quiñones, W. Vallejo and F. Mesa, "Physical and electrochemical study of platinum thin films deposited by sputtering and electrochemical methods", *Appl. Surf. Sci.* **257** (2011) 7545-7550.

[66] N. Papageorgiou, W. F. Maier and M. Grätzel, "An iodine/triiodide reduction electrocatalyst for aqueous and organic media", *J. Electrochem. Soc.* **144** (1997) 876-884.

[67] A. Kay and M. Grätzel, "Low cost photovoltaic modules based on dye sensitized nanocrystalline titanium dioxide and carbon powder", *Sol. Energ. Mat. Sol. C.* **44** (1996) 99-117.

[68] L. Bay, K. West, B. Winther-Jensen and T. Jacobsen, "Electrochemical reaction rates in a dye-sensitised solar cell—the iodide/tri-iodide redox system", *Sol. Energ. Mat. Sol. C.* **90** (2006) 341-351.

[69] H. Choi , H. Kim , S. Hwang, Y. Han and M. Jeon, "Graphene counter electrodes for dye-sensitized solar cells prepared by electrophoretic deposition", *J. Mater. Chem.* **21** (2011) 7548-7551.

[70] H. Wang and Y. H. Hu, "Graphene as a counter electrode material for dye-sensitized solar cells", *Energy Environ. Sci.* **5** (2012) 8182-8188.

[71] G. Wolfbauer, A. M. Bond, J. C. Eklund and D. R. MacFarlane, "A channel flow cell system specifically designed to test the efficiency of redox shuttles in dye sensitized solar cells", *Sol. Energ. Mater. Sol. C.* **70** (2001) 85-101.

[72] A. Yella, H.-W. Lee, H. N. Tsao, C. Yi, A. K. Chandiran, M. K. Nazeeruddin, E. W.-G. Diau, C.-Y. Yeh, S. M. Zakeeruddin and M. Grätzel, "Porphyrin-sensitized solar cells with Cobalt (II/III)-based redox electrolyte exceed 12 percent efficiency", *Science* **334** (2011) 629-634.

[73] Z. Yu, N. Vlachopoulos, M. Gorlov and L. Kloo, "Liquid electrolytes for dye-sensitized solar cells", *Dalton Trans.* **40** (2011) 10289-10303.

[74] L. Andrade, S. M. Zakeeruddin, M. K. Nazeeruddin, H. Aguilar Ribeiro, A. Mendes and M. Grätzel, "Influence of sodium cations of N3 dye on the photovoltaic performance and stability of dye-sensitized solar cells", *ChemPhysChem* **10** (2009) 1117-1124.

[75] G. Schlichthörl, S. Y. Huang, J. Sprague and A. J. Frank, "Band edge movement and recombination kinetics in dye-sensitized nanocrystalline TiO_2 solar cells: A study by intensity modulated photovoltage spectroscopy", *J. Phys. Chem. B* **101** (1997) 8141-8155.

[76] C. Zhang, Y. Huang, Z. Huo, S. Chen and S. Dai, "Photoelectrochemical effects of guanidinium thiocyanate on dye-sensitized solar cell performance and stability", *J. Phys. Chem. C* **113** (2009) 21779-21783.

[77] F. Fabregat-Santiago, J. Bisquert, E. Palomares, L. Otero, D. Kuang, S. M. Zakeeruddin and M. Grätzel, "Correlation between photovoltaic performance and impedance spectroscopy of dye-sensitized solar cells based on ionic liquids", *J. Phys. Chem. C* **111** (2007) 6550-6560.

[78] K. Murakoshi, R. Kogure, and S. Yanagida, "Solid state dye-sensitized TiO_2 solar cell with polypyrrole as hole transport layer", *Chem. Lett.* **5** (1997) 471-472.

[79] Y. Saito, T. Kitamura, Y. Wada and S. Yanagida, "Poly(3,4-ethylenedioxythiophene) as a hole conductor in solid state dye sensitized solar cells", *Synth. Met.* **131** (2002) 185-187.

[80] P. Ravirajan, A. M. Peiró, M. K. Nazeeruddin, M. Graetzel, D. D. C. Bradley, J. R. Durrant and J. Nelson, "Hybrid polymer/zinc oxide photovoltaic devices with vertically oriented ZnO nanorods and an amphiphilic molecular interface layer", *J. Phys. Chem. B* **110** (2006) 7635-7639.

[81] O. Kohle, M. Grätzel, A. F. Meyer and T. B. Meyer, "The photovoltaic stability of, bis(isothiocyanato)rlutheniurn(II)-bis-2, 2´bipyridine-4, 4´-dicarboxylic acid and related sensitizers", *Adv. Mater.* **9** (1997) 904-906.

[82] F. Nour-Mohhamadi, S.D. Nguyen, G. Boschloo, A. Hagfeldt and T. Lund, "Determination of the light-induced degradation rate of the solar cell sensitizer N719 on TiO_2 nanocrystalline particles", *J. Phys. Chem. B* **109** (2005) 22413-22419.

[83] P. J. Cameron and L. M. Peter, "Characterization of titanium dioxide blocking layers in dye-sensitized nanocrystalline solar cells", *J. Phys. Chem. B* **107** (2003) 14394-14400.

[84] D. Kuang, S. Ito, B. Wenger, C. Klein, J.-E. Moser, R. Humphry-Baker, S. M. Zakeeruddin and M. Grätzel, "High molar extinction coefficient heteroleptic ruthenium complexes for thin film dye-sensitized solar cells", *J. Am. Chem. Soc.* **128** (2006) 4146-4154.

[85] A. Hagfeldt and M. Grätzel, "Molecular photovoltaics", *Acc. Chem. Res.* **33** (2000) 269-277.

[86] Y. Tachibana, M. K. Nazeeruddin, M. Grätzel, D. R. Klug and J. R. Durrant, "Electron injection kinetics for the nanocrystalline TiO_2 films sensitised with the dye $(Bu_4N)_2Ru(dcbpyH)_2(NCS)_2$", *Chem. Phys.* **285** (2002) 127-132.

[87] P. Wang, B. Wenger, R. Humphry-Baker, J.-E. Moser, J. Teuscher, W. Kantlehner, J. Mezger, E. V. Stoyanov, S. M. Zakeeruddin and M. Grätzel, "Charge separation and efficient light energy conversion in sensitized mesoscopic solar cells based on binary ionic liquids", *J. Am. Chem. Soc.* **127** (2005) 6850-6856.

[88] B. O'Regan, J. Moser, M. Anderson and M. Grätzel, "Vectorial electron injection into transparent semiconductor membranes and electric field effects on the dynamics of light-induced charge separation", *J. Phys. Chem.* **94** (1990) 8720-8726.

[89] J. Bisquert and V. S. Vikhrenko, "Interpretation of the time constants measured by kinetic techniques in nanostructured semiconductor electrodes and dye-sensitized solar cells", *J. Phys. Chem. B* **108** (2004) 2313-2322.

[90] H. Nusbaumer, S. M. Zakeeruddin, J.-E. Moser and M. Grätzel, "An alternative efficient redox couple for the dye-sensitized solar cell system", *Chem. Eur. J.* **9** (2003) 3756-3763.

[91] L. Han, N. Koide, Y. Chiba, A. Islam, R. Komiya, N. Fuke, A. Fukui and R. Yamanaka, "Improvement of efficiency of dye-sensitized solar cells by reduction of internal resistance ", *Appl. Phys. Lett.* **86** (2005) 213501.

[92] X. Yang, M. Yanagida and L. Han, "Reliable evaluation of dye-sensitized solar cells", *Energy Environ. Sci.* **6** (2013) 54-66.

[93] P. R. F. Barnes, A. Y. Anderson, S. E. Koops, J. R. Durrant and B. C. O'Regan, "Electron injection efficiency and diffusion length in Dye-Sensitized Solar Cells derived from Incident Photon Conversion Efficiency measurements", *J. Phys. Chem. C* **113** (2008) 1126-1136.

[94] X.-Z. Guo, Y.-H. Luo, Y.-D. Zhang, X.-C. Huang, D.-M. Li and Q.-B. Meng, "Study on the effect of measuring methods on incident photon-to-electron conversion efficiency of dye-sensitized solar cells by home-made setup", *Rev. Sci. Instrum.* **81** (2010) 103106.

[95] P. M. Sommeling, H. C. Rieffe, J. A. M. van Roosmalen, A. Schönecker, J. M. Kroon, J. A. Wienke and A. Hinsch, "Spectral response and IV-characterization of dye-sensitized nanocrystalline TiO_2 solar cells", *Sol. Energ. Mater. Sol. C.* **62** (2000) 399-410.

[96] J. Halme, G. Boschloo, A. Hagfeldt and P. Lund, "Spectral characteristics of light harvesting, electron injection, and steady-state charge collection in pressed TiO_2 Dye Solar Cells", *J. Phys. Chem. C* **112** (2008) 5623-5637.

[97] X. Guogang, Y. Xirui, Y. Tao, B. Chunxiong, Z. Jiyuan, G. Jie, H. Huan, T. Zekun and Z. Zhigang, "Understanding of the chopping frequency effect on IPCE measurements for dye-sensitized solar cells: from the viewpoint of electron transport and extinction spectrum", *J. Phys. D Appl. Phys.* **45** (2012) 425104.

[98] L. Dloczik, O. Ileperuma, I. Lauermann, L. M. Peter, E. A. Ponomarev, G. Redmond, N. J. Shaw and I. Uhlendorf, "Dynamic response of Dye-Sensitized Nanocrystalline Solar Cells: characterization by Intensity-Modulated Photocurrent Spectroscopy", *J. Phys. Chem. B* **101** (1997) 10281-10289.

[99] G. Schlichthörl, N. G. Park and A. J. Frank, "Evaluation of the charge-collection efficiency of Dye-Sensitized Nanocrystalline TiO_2 Solar Cells", *J. Phys. Chem. B* **103** (1999) 782-791.

[100] S. Nakade, T. Kanzaki, Y. Wada and S. Yanagida, "Stepped light-induced transient measurements of photocurrent and voltage in Dye-Sensitized Solar Cells: application for highly viscous electrolyte systems", *Langmuir* **21** (2005) 10803-10807.

[101] G. Schlichthörl, S. Y. Huang, J. Sprague and A. J. Frank, "Band edge movement and recombination kinetics in Dye-Sensitized Nanocrystalline TiO_2 Solar Cells: a study by Intensity Modulated Photovoltage Spectroscopy", *J. Phys. Chem. B* **101** (1997) 8141-8155.

[102] A. Zaban, M. Greenshtein and J. Bisquert, "Determination of the electron lifetime in nanocrystalline Dye Solar Cells by Open-Circuit Voltage Decay measurements", *ChemPhysChe*m **4** (2003) 859-864.

[103] N. W. Duffy, L. M. Peter, R. M. G. Rajapakse and K. G. U. Wijayantha, "Investigation of the kinetics of the back reaction of electrons with tri-iodide in dye-sensitized nanocrystalline photovoltaic cells", *J. Phys. Chem. B* **104** (2000) 8916-8919.

[104] J. R. Macdonald, "Impedance spectroscopy", *Ann. Biomed. Eng.* **20** (1992) 289-305.

[105] Q. Wang, J. E. Moser and M. Grätzel, “Electrochemical impedance spectroscopic analysis of dye-sensitized solar cells”, *J. Phys. Chem. B* **109** (2005) 14945-14953.

[106] J. Halme, P. Vahermaa, K. Miettunen and P. Lund, “Device physics of dye solar cells”, *Adv. Mater.* **22** (2010) E210-E234.

[107] F. Fabregat-Santiago, J. Bisquert, G. Garcia-Belmonte, G. Boschloo and A. Hagfeldt, "Influence of electrolyte in transport and recombination in dye-sensitized solar cells studied by impedance spectroscopy", *Sol. Energ. Mater. Sol. C.* **87** (2005) 117-131.

[108] J. Bisquert, G. Garcia-Belmonte, F. Fabregat-Santiago, N. S. Ferriols, P. Bogdanoff and E. C. Pereira, "Doubling exponent models for the analysis of porous film electrodes by impedance. Relaxation of TiO_2 nanoporous in aqueous solution", *J. Phys. Chem. B* **104** (2000) 2287-2298.

[109] P. M. Sommeling, B. C. O’Regan, R. R. Haswell, H. J. P. Smit, N. J. Bakker, J. J. T. Smits, J. M. Kroon and J. A. M. van Roosmalen, "Influence of a $TiCl_4$ Post-Treatment on Nanocrystalline TiO_2 Films in Dye-Sensitized Solar Cells", *J. Phys. Chem. B* **110** (2006) 19191-19197.

[110] R. Gazia, A. Chiodoni, S. Bianco, A. Lamberti, M. Quaglio, A. Sacco, E. Tresso, P. Mandracci and C. F. Pirri, "An easy method for the room-temperature growth of spongelike nanostructured Zn films as initial step for the fabrication of nanostructured ZnO", *Thin Solid Films* **524** (2012) 107-112.

[111] A. Lamberti, A. Sacco, S. Bianco, D. Manfredi, F. Cappelluti, S. Hernandez, M. Quaglio and C. F. Pirri, "Charge transport improvement employing TiO_2 nanotube arrays as front-side illuminated dye-sensitized solar cell photoanodes", *Phys. Chem. Chem. Phys.* **15** (2013) 2596-2602.

[112] V. I. Nizhenko, V. N. Eremenko and L. I. Sklyarenko, "Application of the sessile drop method to the determination of the surface energy and density of liquids wetting the backing material", *Powder Metall. Met. Ceram.* **4** (1965) 463-466.

[113] D. J. Dahm and K. D. Dahm, "Interpreting diffuse reflectance and transmittance", (2007) NIR Publications, Chichester.

[114] G. M. Whitesides, "The origins and the future of microfluidics", *Nature* **442** (2006) 368-373.

[115] S. Saleh-Lakha and J. T. Trevors, "Perspective: microfluidic applications in microbiology", *J. Microbiol. Methods* **82** (2010) 108-111.

[116] S. Pennathur, J.C.T. Eijkel and A. van den Berg, "Energy conversion in microsystems: is there a role for micro/nanofluidics?", *Lab Chip* **7** (2007) 1234-1237.

[117] S. Marasso, E. Giuri, G. Canavese, R. Castagna, M. Quaglio, I. Ferrante, D. Perrone and M. Cocuzza, "A multilevel Lab on chip platform for DNA analysis", *Biomed. Microdevices* **13** (2011) 19-27.

[118] Q. Wang, S. Ito, M. Grätzel, F. Fabregat-Santiago, I. Mora-Seró, J. Bisquert, T. Bessho and H. Imai, "Characteristics of high efficiency Dye-Sensitized Solar Cells", *J. Phys. Chem. B* **110** (2006) 25210-25221.

[119] H. Imahori, T. Umeyama and S. Ito, "Large π-aromatic molecules as potential sensitizers for highly efficient Dye-Sensitized Solar Cells", *Acc. Chem. Res.* **42** (2009) 1809-1818.

[120] J. Park, C. Barolo, F. Sauvage, N. Barbero, C. Benzi, P. Quagliotto, S. Coluccia, D. Di Censo, M. Grätzel, M. K. Nazeeruddin and G. Viscardi, "Symmetric vs. asymmetric squaraines as photosensitisers in mesoscopic injection solar cells: a structure-property relationship study", *Chem. Commun.* **48** (2012) 2782-2784.

[121] M. Matsui, H. Mase, J.-Y. Jin, K. Funabiki, T. Yoshida and H. Minoura, "Application of semisquaric acids as sensitizers for zinc oxide solar cell", *Dyes Pigment.* **70** (2006) 48-53.

[122] M. Guo, P. Diao, Y.-J. Ren, F. Meng, H. Tian and S.-M. Cai, "Photoelectrochemical studies of nanocrystalline TiO_2 co-sensitized by novel cyanine dyes", *Sol. Energ. Mater. Sol. C.* **88** (2005) 23-35.

[123] J. A. Mikroyannidis, P. Suresh, M. S. Roy and G. D. Sharma, "New photosensitizer with phenylenebisthiophene central unit and cyanovinylene 4-nitrophenyl terminal units for dye-sensitized solar cells", *Electrochim. Acta* **56** (2011) 5616-5623.

[124] T. Ono, T. Yamaguchi and H. Arakawa, "Study on dye-sensitized solar cell using novel infrared dye", *Sol. Energ. Mater. Sol. C.* **93** (2009) 831-835.

[125] H.-M. Cheng, W.-H. Chiu, C.-H. Lee, S.-Y. Tsai and W.-F. Hsieh, "Formation of branched ZnO nanowires from solvothermal method and Dye-Sensitized Solar Cells applications", *J. Phys. Chem. C* **112** (2008) 16359-16364.

[126] M. J. Bierman and S. Jin, "Potential applications of hierarchical branching nanowires in solar energy conversion", *Energy Environ. Sci.* **2** (2009) 1050-1059.

[127] K. Keis, J. Lindgren, S.-E. Lindquist and A. Hagfeldt, "Studies of the adsorption process of Ru complexes in nanoporous ZnO electrodes", *Langmuir* **16** (2000) 4688-4694.

[128] H. Horiuchi, R. Katoh, K. Hara, M. Yanagida, S. Murata, H. Arakawa and M. Tachiya, "Electron injection efficiency from excited N3 into nanocrystalline ZnO films: effect of (N3-Zn^{2+}) aggregate formation", *J. Phys. Chem. B* **107** (2003) 2570-2574.

[129] I. Gonzalez-Valls and M. Lira-Cantu, "Vertically-aligned nanostructures of ZnO for excitonic solar cells: a review", *Energy Environ. Sci.* **2** (2009) 19-34.

[130] M. A. Baker, W. Gissler, S. Klose, M. Trampert and F. Weber, "Morphologies and corrosion properties of PVD Zn-Al coatings", *Surf. Coat. Technol.* **125** (2000) 207-211.

[131] A. F. Jankowski and J. P. Hayes, "Sputter deposition of a spongelike morphology in metal coatings", *J. Vac. Sci. Technol. A* **21** (2003) 422-425.

[132] J. Musil, J. Matouš and V. Valvoda, "Effect of ion bombardment on the surface morphology of Zn-films sputtered in an unbalanced magnetron", *Vacuum* **46** (1995) 203-210.

[133] P. J. Cameron and L. M. Peter, "How does back-reaction at the conducting glass substrate influence the dynamic photovoltage response of nanocrystalline Dye-Sensitized Solar Cells?", *J. Phys. Chem. B* **109** (2005) 7392-7398.

[134] S. M. Waita, B. O. Aduda, J. M. Mwabora, C. G. Granqvist, S.-E. Lindquist, G. A. Niklasson, A. Hagfeldt and G. Boschloo, "Electron transport and recombination in Dye Sensitized Solar Cells fabricated from obliquely sputter deposited and thermally annealed TiO_2 films", *J. Electroanal. Chem.* **605** (2007) 151-156 .

[135] V. Zwilling, M. Aucouturier and E. Darque-Ceretti, "Anodic oxidation of titanium and TA6V alloy in chromic media. An electrochemical approach", *Electrochim. Acta* **45** (1999) 921-929.

[136] G. Liu, K. Wang, N. Hoivik and H. Jakobsen, "Progress on free-standing and flow-through TiO_2 nanotube membranes", *Sol. Energ. Mat. Sol. C.* **98** (2012) 24-38.

[137] P. Roy, S. Berger and P. Schmuki, "TiO_2 nanotubes: synthesis and applications", *Angew. Chem. Int. Edit.* **50** (2011) 2904-2939.

[138] J. M. Macak, H. Tsuchiya, L. Taveira, S. Aldabergerova and P. Schmuki, "Smooth anodic TiO_2 nanotubes", *Angew. Chem. Int. Edit.* **44** (2005) 7463-7465.

[139] J. Yan and F. Zhou, "TiO_2 nanotubes: structure optimization for solar cells", *J. Mater. Chem.* **21** (2011) 9406-9418.

[140] B. C. O'Regan, J. R. Durrant, P. M. Sommeling and N. J. Bakker, "Influence of the $TiCl_4$ treatment on nanocrystalline TiO_2 films in Dye-Sensitized Solar Cells. 2. Charge density, band edge shifts, and quantification of recombination losses at short circuit", *J. Phys. Chem. C* **111** (2007) 14001-14010.

[141] H. Wang, M. Liu, M. Zhang, P. Wang, H. Miura, Y. Cheng and J. Bell, "Kinetics of electron recombination of dye-sensitized solar cells based on TiO_2 nanorod arrays sensitized with different dyes", *Phys. Chem. Chem. Phys.* **13** (2011) 17359-17366.

[142] R. Harikisun and H. Desilvestro, "Long-term stability of dye solar cells", *Sol. Energy* **85** (2011) 1179-1188.

[143] A. Hinsch, J. M. Kroon, R. Kern, I. Uhlendorf, J. Holzbock, A. Meyer and J. Ferber, "Long-term stability of dye-sensitised solar cells", *Prog. Photovolt. Res. Appl.* **9** (2001) 425-438.

[144] B. Macht, M. Turrión, A. Barkschat, P. Salvador, K. Ellmer and H. Tributsch, "Patterns of efficiency and degradation in dye sensitization solar cells measured with imaging techniques", *Sol. Energ. Mat. Sol. C.* **73** (2002) 163-173.

[145] E. Olsen, G. Hagen and S. E. Lindquist, "Dissolution of platinum in methoxy propionitrile containing LiI/I_2", *Sol. Energ. Mat. Sol. C.* **63** (2000) 267-273.

[146] H. G. Agrell, J. Lindgren and A. Hagfeldt, "Degradation mechanisms in a dye-sensitized solar cell studied by UV-VIS and IR spectroscopy", *Sol. Energy* **75** (2003) 169-180.

[147] H.-L. Lu, T. F. R. Shen, S.-T. Huang, Y.-L. Tung and T. C. K. Yang, "The degradation of dye sensitized solar cell in the presence of water isotopes", *Sol. Energ. Mat. Sol. C.* **95** (2011) 1624-1629.

[148] Y. Liu, A. Hagfeldt, X.-R. Xiao and S.-E. Lindquist, "Investigation of influence of redox species on the interfacial energetics of a dye-sensitized nanoporous TiO_2 solar cell", *Sol. Energ. Mat. Sol. C.* **55** (1998) 267-281.

[149] M. Toivola, L. Peltokorpi, J. Halme and P. Lund, "Regenerative effects by temperature variations in dye-sensitized solar cells", *Sol. Energ. Mat. Sol. C.* **91** (2007) 1733-1742.

[150] A. Fattori, L. M. Peter, S. R. Belding, R. G. Compton and F. Marken, "*Cis*-bis(isothiocyanato)-bis(2,2´-bipyridyl-4,4´dicarboxylato)-Ru(II) (N719) dark-reactivity when bound to fluorine-doped tin oxide (FTO) or titanium dioxide (TiO_2) surfaces", *J. Electroanal. Chem.* **640** (2010) 61-67.

[151] B. Enright, G. Redmond and D. Fitzmaurice, "Spectroscopic determination of flatband potentials for polycrystalline TiO_2 electrodes in mixed solvent systems", *J. Phys. Chem.* **98** (1994) 6195-6200.

[152] A. Usami, S. Seki, Y. Mita, H. Kobayashi, H. Miyashiro and N. Terada, "Temperature dependence of open-circuit voltage in dye-sensitized solar cells", *Sol. Energ. Mat. Sol. C.* **93** (2009) 840-842.

List of publications

1. A. Lamberti, A. Sacco, S. Bianco, E. Giuri, M. Quaglio, A. Chiodoni, E. Tresso, "Microfluidic sealing and housing system for innovative dye sensitized solar cell architecture", *Microelectron. Eng.* **88**, 2308 (2011).

2. A. Sacco, A. Lamberti, M. Quaglio, S.Bianco, E. Tresso, A.-L. Alexe-Ionescu, C.F. Pirri, "Electric characterization and modeling of microfluidic-based dye sensitized solar cell", *Int. J. Photoenergy* **2012**, Art. ID 216780 (2012).

3. A. Lamberti, M. Quaglio, A. Sacco, M. Cocuzza, C. F. Pirri, "Surface energy tailoring of glass substrate by contact printed PDMS", *Appl. Surf. Sci.* **258**, 9427 (2012).

4. A. Sacco, A. Lamberti, D. Pugliese, A. Chiodoni, N. Shahzad, S. Bianco, M. Quaglio, R. Gazia, E. Tresso, C. F. Pirri, "Microfluidic housing system: a useful tool for the analysis of dye-sensitized solar cell components", *Appl. Phys. A - Mater. Sci. Process.* **109**, 377 (2012).

5. A. Sacco, A. Lamberti, R. Gazia, S. Bianco, D. Manfredi, N. Shahzad, F. Cappelluti, S. Ma, E. Tresso, "High efficiency Dye-sensitized Solar Cell exploiting sponge-like ZnO nanostructures", *Phys. Chem. Chem. Phys.* **14**, 16203 (2012).

6. R. Gazia, A. Chiodoni, S. Bianco, A. Lamberti, M. Quaglio, A. Sacco, E. Tresso, P. Mandracci, C. F. Pirri, "An easy method for the room-temperature growth of spongelike nanostructured Zn films as initial step for the fabrication of nanostructured ZnO", *Thin Solid Films* **524**, 107 (2012).

7. A. Sacco, L. Rolle, L. Scaltrito, E. Tresso, C. F. Pirri, "Characterization of photovoltaic modules for low-power indoor application", *Appl. Energ.* **102**, 1295 (2013).

8. A. Lamberti, A. Sacco, S. Bianco, D. Manfredi, F. Cappelluti, S. Hernandez, M. Quaglio, C. F. Pirri, "Charge transport improvement employing TiO_2 nanotube array as front-side illuminated Dye-sensitized Solar Cell photoanode", *Phys. Chem. Chem. Phys.* **15**, 2596 (2013).

9. F. Bella, D. Pugliese, J. R. Nair, A. Sacco, S. Bianco, C. Gerbaldi, C. Barolo, R. Bongiovanni, "UV-crosslinked polymer electrolyte membranes for quasi-solid dye-sensitized solar cells with excellent efficiency and durability", *Phys. Chem. Chem. Phys.* **15**, 3706 (2013).

10. A. Lamberti, A. Sacco, D. Hidalgo, S. Bianco, D. Manfredi, M. Quaglio, E. Tresso, C. F. Pirri, "TiO_2 nanotube array as efficient transparent photoanode in Dye-sensitized Solar Cell with high electron lifetime", *Acta Phys. Pol. A* **123**, 376 (2013).

11. A. Sacco, A. Lamberti, I. Berardone, S. Bianco, R. Gazia, D. Pugliese, M. Quaglio, E. Tresso, C. F. Pirri, "Spongelike porous ZnO photoanodes for highly efficient Dye Sensitized Solar Cells", *Acta Phys. Pol. A* **123**, 386 (2013).

12. A. Lamberti, R. Gazia, A. Sacco, S. Bianco, M. Quaglio, A. Chiodoni, E. Tresso, C. F. Pirri, "Coral-shaped ZnO nanostructures as Dye Sensitized Solar Cell photoanodes", *Prog. Photovolt: Res. Appl.*, in press (doi: 10.1002/pip.2251).

13. F. Cappelluti, S. Ma, D. Pugliese, A. Sacco, A. Lamberti, G. Ghione, E. Tresso, "Consistent static and small-signal physics-based modeling of dye-sensitized solar cells under different illumination conditions", *Phys. Chem. Chem. Phys.*, in press (doi: 10.1039/C3CP43802C).

14. R. Gazia, G. Canavese, A. Chiodoni, A. Lamberti, S. Stassi, A. Sacco, S. Bianco, A. Virga, E. Tresso, C. F. Pirri, "Novel spongelike nanostructured ZnO films: properties and applications", *J. Alloy. Compd.*, in press (doi: 10.1016/j.jallcom.2013.01.149).

15. G. Cicero, G. Musso, A. Lamberti, B. Camino, S. Bianco, D. Pugliese, F. Risplendi, A. Sacco, N. Shahzad, A. M. Ferrari, B. Ballarin, C. Barolo, E. Tresso, G. Caputo, "Combined experimental and theoretical investigation of the hemi-squaraine/TiO_2 interface for dye sensitized solar cells", *Phys. Chem. Chem. Phys.,* in press (doi: 10.1039/C3CP50559F).

16. A. Lamberti, A. Sacco, S. Bianco, M. Quaglio, D. Manfredi, C. F. Pirri, "Enhancement of electron lifetime in Dye-sensitized Solar Cell using anodically grown TiO_2 nanotube/nanoparticle composite photoanodes", *Microelectron. Eng.*, accepted.